

Integrated view of internal friction in unfolded proteins from single-molecule FRET, contact quenching, theory, and simulations

Andrea Soranno^{a,1,2}, Andrea Holla^a, Fabian Dingfelder^a, Daniel Nettels^a, Dmitrii E. Makarov^{b,c}, and Benjamin Schuler^{a,d,2}

^aDepartment of Biochemistry, University of Zurich, 8057 Zurich, Switzerland; ^bDepartment of Chemistry, University of Texas at Austin, Austin, TX 78712; ^cInstitute for Computational Engineering and Sciences, University of Texas at Austin, Austin, TX 78712; and ^dDepartment of Physics, University of Zurich, 8057 Zurich, Switzerland

Edited by Attila Szabo, National Institutes of Health, Bethesda, MD, and approved January 25, 2017 (received for review October 31, 2016)

Internal friction is an important contribution to protein dynamics at all stages along the folding reaction. Even in unfolded and intrinsically disordered proteins, internal friction has a large influence, as demonstrated with several experimental techniques and in simulations. However, these methods probe different facets of internal friction and have been applied to disparate molecular systems, raising questions regarding the compatibility of the results. To obtain an integrated view, we apply here the combination of two complementary experimental techniques, simulations, and theory to the same system: unfolded protein L. We use single-molecule Förster resonance energy transfer (FRET) to measure the global reconfiguration dynamics of the chain, and photoinduced electron transfer (PET), a contact-based method, to quantify the rate of loop formation between two residues. This combination enables us to probe unfolded-state dynamics on different length scales, corresponding to different parts of the intramolecular distance distribution. Both FRET and PET measurements show that internal friction dominates unfolded-state dynamics at low denaturant concentration, and the results are in remarkable agreement with recent large-scale molecular dynamics simulations using a new water model. The simulations indicate that intrachain interactions and dihedral angle rotation correlate with the presence of internal friction, and theoretical models of polymer dynamics provide a framework for interrelating the contribution of internal friction observed in the two types of experiments and in the simulations. The combined results thus provide a coherent and quantitative picture of internal friction in unfolded proteins that could not be attained from the individual techniques.

single-molecule FRET | nanosecond FCS | PET quenching | Rouse model with internal friction | intrinsically disordered proteins

The dynamics and folding of proteins are often modeled as a diffusive process on a free-energy surface (1–3). In contrast to simpler rate processes in the condensed phase (4), however, protein dynamics are often much slower than expected from solvent friction alone. This behavior indicates that solvent molecules are not the only cause of friction, but that other sources (commonly referred to as “internal,” in contrast to the “external” action of the solvent) control protein relaxation (5–12). Internal friction has been reported for native-state dynamics (9) and folding kinetics, especially for proteins folding in the microsecond range (6, 13), but even for proteins folding in milliseconds (11), suggesting the presence of a solvent-independent frictional component in the transition-state ensemble (10, 13, 14).

The simplest mechanistic explanation for internal friction in native proteins and transition states is that in these rather compact configurations, a large fraction of the protein atoms is not fully exposed to the solvent, and is therefore dominated by collisions and interactions with other parts of the protein (9), involving predominantly small-amplitude motions, where little solvent is displaced (15). It thus came as a surprise when recent experiments and simulations demonstrated that internal friction can dominate even the dynamics of unfolded and intrinsically disordered proteins and peptides (10, 12, 16–22), which are more expanded and

accessible to solvent. In both experiments (10, 12, 16, 17) and simulations (19–21), unfolded proteins often exhibit the characteristic signature of internal friction: a pronounced deviation from direct proportionality of their reconfiguration times to solvent viscosity. The underlying molecular mechanisms, however, have remained unclear. Recent single-molecule experiments indicate a correlation of internal friction with chain compaction, suggestive of attractive intrachain interactions slowing dynamics (12, 23). However, the magnitude of internal friction was found to be only weakly dependent on chain segment length and bisection of an unfolded protein, pointing to a molecular origin that is rather independent of local sequence-specific effects (12). Molecular dynamics (MD) simulations have proven particularly important for connecting experimental observations to molecular details and for investigating protein dynamics in low-viscosity regimes that are experimentally inaccessible (19–21, 24, 25). Based on these studies, different molecular contributions to internal friction have been proposed, including hydrogen bonds (19), nonnative salt bridges (14), concerted dihedral rotations involving crank-shaft motions of the polypeptide backbone (21), and differences in native-state topology (24). Deviations from direct proportionality of relaxation times and solvent viscosity can also be due to inertial effects or solvent memory in dihedral angle hopping (20, 25, 26).

A way of testing our understanding of internal friction in unfolded proteins is the use of experimental data from complementary techniques that probe chain dynamics on different length and time scales. For instance, single-molecule experiments based on

Significance

The dynamics of proteins, which are essential for both folding and function, are known to be strongly dependent on solvent viscosity and friction. However, an increasing number of experiments have demonstrated the importance of a contribution to protein dynamics independent of solvent friction. Such “internal friction” has recently been detected even in unfolded proteins, although they are more expanded and solvent-accessible than folded proteins. Based on two complementary experimental methods, simulations, and theory, our results provide a coherent view of internal friction in unfolded proteins and constitute an important basis for understanding the molecular origin of this phenomenon and its role for the folding of proteins and for the functional dynamics of intrinsically disordered proteins.

Author contributions: A.S. and B.S. designed research; A.S., A.H., and F.D. performed research; D.N. and D.E.M. contributed new reagents/analytic tools; A.S. analyzed data; and A.S., D.E.M., and B.S. wrote the paper.

The authors declare no conflict of interest.

This article is a PNAS Direct Submission.

¹Present address: Department of Biochemistry and Molecular Biophysics, Washington University in St. Louis, St. Louis, MO 63110.

²To whom correspondence may be addressed. Email: schuler@bioc.uzh.ch or soranno@wustl.edu.

This article contains supporting information online at www.pnas.org/lookup/suppl/doi:10.1073/pnas.1616672114/-DCSupplemental.

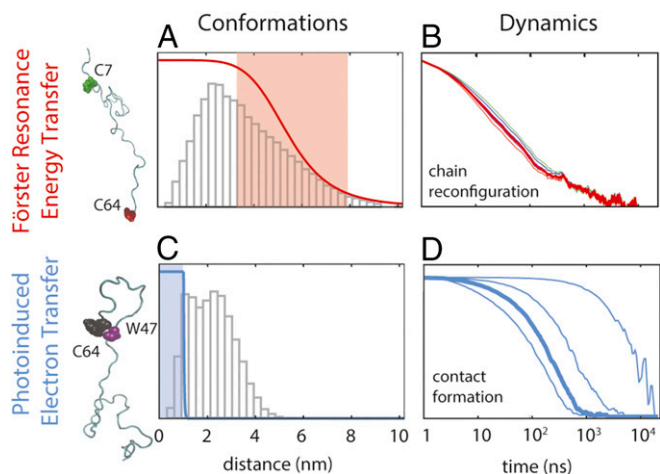


Fig. 1. Investigating the conformations and dynamics of protein L using FRET and PET. FRET is most sensitive in a range of distances close to the Förster radius (A; $\sim 5.4 \pm 3$ nm, shaded in red), whereas PET is only effective at distances smaller than the contact radius (C; < 1 nm, shaded in blue). The distance dependencies of the transfer efficiency and the relative electron transfer rate are shown as red and blue lines in A and C (ranging from 1 to 0), respectively, superimposed on the distance distributions of the segments probed by FRET (C7–C64) and PET (W47–C64) from an 86- μ s MD simulation of unfolded protein L (31) (gray histograms). Decays of correlations for chain reconfiguration (B) and contact formation (D) are based on the MD simulation (31). (B) Typical reconfiguration times for a sequence separation of 57 amino acids occur on a time scale of 10–100 ns and show a very weak dependence on the Förster radius (correlation curves shown for Förster radii of 5.0, 5.2, 5.4, 5.6, 5.8, and 6.0 nm, respectively). (D) In contrast, contact formation is very sensitive to the contact radius (from left to right, R_c is 1.0, 0.8, 0.6, and 0.4 nm, respectively), and therefore can differ by orders of magnitude depending on the probes used (from 100 ns to 10 μ s for the 18-residue segment investigated here).

Förster resonance energy transfer (FRET) combined with nanosecond fluorescence correlation spectroscopy (nsFCS) on several unfolded proteins have revealed reconfiguration dynamics of 30- to 100-residue chain segments on time scales between about 10 ns and 100 ns (10, 12, 16, 27). In contrast, loop formation detected in contact-based measurements between Cys and Trp in a 10-residue segment within unfolded protein L was reported to occur on much slower time scales, between 1 μ s and 10 μ s (18). The different distance dependencies for the rates of FRET ($\propto 1/r^6$) and contact formation ($\propto e^{-r}$) and the resulting sensitivity to distance changes on different length scales provide an excellent opportunity for probing the effect of internal friction on different parts of the intramolecular distance distribution (28), corresponding to more extended versus compact conformations within the unfolded-state ensemble (Fig. 1). Comparing such experiments directly with simulations has been very challenging, both because of the high computational demands for all-atom explicit solvent simulations of unfolded proteins on the required time scales and because of the lack of force fields that provide a realistic description of the unfolded state and do not lead to overly compact chains. Recent advances in computational power (29, 30) and force field development (31–35) have started to change this situation.

Here, we use the combination of single-molecule FRET-based and contact-based experiments on protein L and compare them with recent long-time scale atomistic simulations from Shaw and coworkers (31) and with the predictions of a polymer model that includes internal friction effects (36) to elucidate whether internal friction observed on different time and length scales can be explained with a consistent theoretical view.

Results

Conformational Ensemble of Unfolded Protein L. The quantitative interpretation of nanosecond relaxation times obtained by the combination of FRET with nsFCS (FRET-FCS) requires in-

formation about the conformational distribution sampled by the chain. We labeled the double-Cys variant K7CG64C of protein L with Alexa 488 and Alexa 594 as donor and acceptor fluorophores, respectively (SI Appendix and SI Appendix, Table S1; Förster radius: 5.4 nm), and used single-molecule FRET to estimate the dimensions of the unfolded state at different guanidinium chloride (GdmCl) concentrations. In the resulting FRET efficiency histograms (Fig. 2A), we observed three peaks: one at $E \approx 0.9$, which corresponds to the folded state of the protein; one with E between 0.5 and 0.8, corresponding to the unfolded state; and one at a transfer efficiency of $E \approx 0$, from molecules without active acceptor dye. The areas of the corresponding transfer efficiency peaks yield the relative populations of folded and unfolded states (Fig. 2C). With increasing GdmCl concentration, the unfolded state is increasingly populated, and its peak shifts from higher to lower transfer efficiency (Fig. 2B), reflecting chain expansion, as observed previously for protein L (37–39) and many other proteins (23, 40, 41).

The RMS internal distance between the labeling sites, $R_{7,64}$, in the unfolded state (Fig. 2B) and the underlying distance distribution can be inferred from the transfer efficiency by using polymer models (23) [e.g., a Gaussian chain (23, 42, 43)], a self-avoiding walk, or a worm-like chain (23) (SI Appendix). The distance distributions

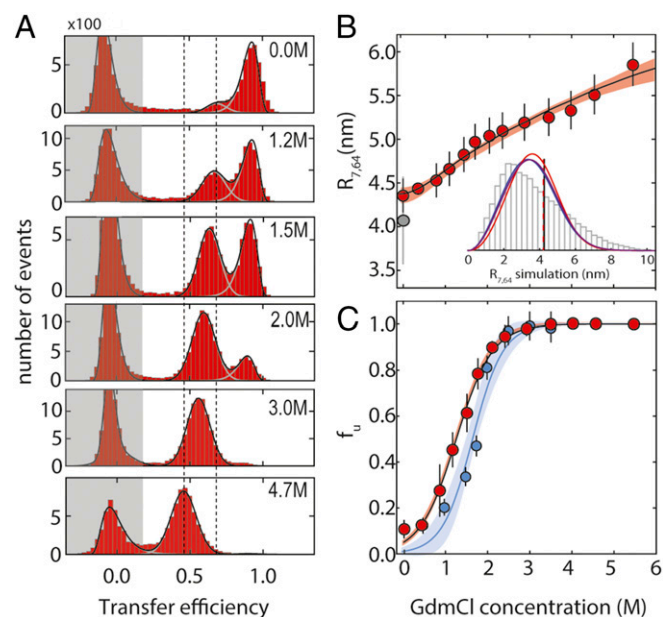


Fig. 2. Single-molecule FRET experiments on protein L stability and unfolded-state dimensions. (A) Examples of FRET efficiency (E) histograms at different GdmCl concentrations (folded state: high E ; unfolded state: intermediate E ; population with inactive acceptor dye: low E , shaded in gray). Vertical dashed lines identify the change in the mean transfer efficiency of the unfolded state between 0 and 4.7 M GdmCl. (B) RMS distance between residues 7 and 64, $R_{7,64}$, as estimated from the transfer efficiencies (SI Appendix) at different denaturant concentrations, fitted to a simple binding model (shaded area corresponds to a 90% confidence interval). Error bars represent the SD from at least two measurements at the same denaturant concentration. The gray-filled circle represents the value of $R_{7,64}$ from the MD simulation (31), with the error bar corresponding to the SD of $R_{7,64}$ when computed from 10- μ s segments of the trajectory. (Inset) Distribution of distances sampled in the MD simulation between residues 7 and 64 compared with three polymer distributions [Gaussian chain (blue), worm-like chain (purple), and self-avoiding walk (red)] that correspond to the same mean transfer efficiency as computed from the MD trajectory. Vertical lines indicate the RMS distances of the distributions (virtually indistinguishable). (C) Fraction of unfolded protein, f_u , according to the relative areas of peaks corresponding to folded and unfolded states in FRET efficiency histograms (red) and f_u obtained from PET experiments (blue) (Fig. 4 and SI Appendix for comparison). Error bars represent the SD from at least two measurements at the same denaturant concentration. Shaded areas represent the 90% confidence interval of the fit.

from the polymer models agree well with the corresponding distributions calculated from the 86- μ s atomistic MD simulation of unfolded protein L in explicit solvent by Piana et al. (31) using the Amber12 force field (44) in combination with the recently developed TIP4P-D water model (31) (Fig. 2B and *SI Appendix*, Fig. S1). Given the similarity of the shapes of the distance distributions of the polymer models (*SI Appendix*, Fig. S1), we use the Gaussian chain, the simplest model, for quantifying chain dimensions over the entire range of GdmCl concentrations (Fig. 2B).

Reconfiguration Dynamics and Internal Friction from Single-Molecule FRET. FRET-FCS reports on protein dynamics that result in distance fluctuations between the dyes (10, 12, 16, 27). The correlation curves for unfolded protein L (Fig. 3A) exhibit the characteristic correlated signal in the autocorrelation functions and anti-correlated signal in the cross-correlation function that are diagnostic of distance fluctuations between donor and acceptor (details are provided in *SI Appendix*). The distance relaxation time corresponding to the reconfiguration of the chain, τ_r (16) (Fig. 2C), is obtained from the fluorescence intensity relaxation time, τ_{CD} , by describing the chain dynamics in terms of diffusion on the potential of mean force obtained by Boltzmann inversion of the distance distribution inferred from the transfer efficiencies (Fig. 2B, *Inset* and *SI Appendix*). With increasing denaturant concentration, τ_r first decreases from 95 ± 15 ns at 0.5 M GdmCl to 45 ± 7 ns at 4 M GdmCl, and then increases again, reaching 60 ± 9 ns at 7 M GdmCl, a behavior similar to that of other proteins of comparable size and sequence composition (10, 12, 16, 27). Remarkably, τ_r calculated directly from the MD trajectory of unfolded protein L yields a value of ~ 110 ns for the dominant dynamic component (Fig. 3B and *SI Appendix*, Fig. S2), which is very close to the experimental value, lending further support to a realistic representation of unfolded-state dynamics in the simulations using the TIP4P-D water model (31). However, the MD-based correlation function reveals residual dynamics up to time scales of several microseconds (*SI Appendix*, Fig. S2), indicating that complete convergence is not achieved even in this 86- μ s simulation. Such slow modes in the relaxation time may reflect the population of local structural elements (hydrogen-bonded turns, bends, and extended segments) (*SI Appendix*, Fig. S2). Our experimental data do not provide direct evidence for dynamics on this time scale, but a low-amplitude component cannot be ruled out owing to experimental uncertainty. Based on photoinduced electron transfer (PET) experiments at low excitation rates, for which the potentially interfering triplet contribution in the microsecond range of the correlation function is particularly low (45), we estimate an upper bound of 10–15% for the contribution of microsecond dynamics, consistent with the simulations.

We have previously shown that in the framework of simple polymer models, such as the Rouse model with internal friction (RIF) or Zimm model with internal friction (ZIF) (36, 46), the reconfiguration time of the chain can be decomposed into two additive components (12)

$$\tau_r = \tau_s + \tau_i \quad [1]$$

[We restrict our data analysis to the RIF model; an analysis based on the ZIF model was previously shown to yield virtually indistinguishable results (12, 36).] Here, τ_s is the reconfiguration time in the absence of internal friction (described by the standard Rouse model), which is thus directly proportional to the solvent viscosity, η_s , and to the mean square interdye distance, R^2 (i.e., $\tau_s \propto R^2 \eta_s$), and τ_i is a time scale that arises from internal friction. Following a previously established procedure (10, 12), we separated τ_s and τ_i for all denaturant concentrations (Fig. 3 and *SI Appendix*). The resulting τ_i (Fig. 3C, purple line) increases from 28 ± 18 ns at 6 M GdmCl to ~ 90 ns under native conditions. We tested the robustness of the extrapolation procedure by directly comparing τ_i with the value measured via the solvent viscosity dependence at a lower denaturant concentration. At 2 M

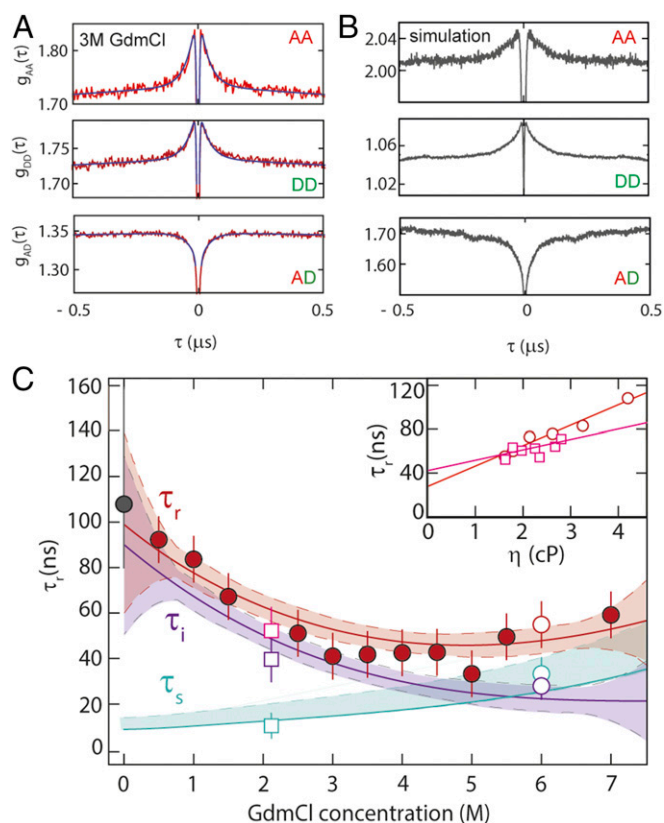


Fig. 3. Probing unfolded-state dynamics by FRET-FCS. (A) Autocorrelation of acceptor fluorescence, $g_{AA}(\tau)$; donor fluorescence, $g_{DD}(\tau)$; and cross-correlation of acceptor and donor fluorescence, $g_{AD}(\tau)$, at 3 M GdmCl; black lines show a global fit of the three correlations, with the reconfiguration time, τ_r , as a shared fit parameter. (B) FRET-FCS correlations $g_{AA}(\tau)$, $g_{DD}(\tau)$, and $g_{AD}(\tau)$ based on the MD trajectory of unfolded protein L (31) (*SI Appendix*). (C) τ_r from the global fit of $g_{AA}(\tau)$, $g_{DD}(\tau)$, and $g_{AD}(\tau)$ (red-filled circles); the internal friction contribution, τ_i (purple line), is obtained by subtracting from the polynomial interpolation curve of τ_r (red line) the solvent component, τ_s (cyan line). The gray-filled circle at 0 M GdmCl represents the reconfiguration time of the chain from the MD simulation (*SI Appendix*). Error bars represent an average relative error of 15%, as estimated from the SD of multiple independent measurements. Confidence intervals (90%) of the fit are represented as shaded areas of the corresponding color. (*Inset*) τ_r at 2.2 M (empty squares) and 6.0 M GdmCl (empty circles) as a function of solution viscosity, η ; linear extrapolation to zero viscosity (Eq. 1) allows τ_s (empty cyan circle and square in main panel) and τ_i (empty purple circle and square in main panel) to be estimated.

GdmCl, the viscosity dependence of τ_r yields τ_i (2 M) $\approx 42 \pm 7$ ns, close to the extrapolated RIF estimate. In summary, in the absence of denaturant, the contribution of internal friction dominates the dynamics of unfolded protein L by an order of magnitude compared to the solvent friction component.

Contact Formation Dynamics from PET-FCS. Our observations thus far are based on the long-range coupling between FRET donor and acceptor, with greatest sensitivity to distance changes in the range of the Förster radius (5.4 nm). To understand how internal friction affects dynamics as monitored by contact formation between two groups within the chain, and thus with greatest sensitivity to distance changes in the subnanometer range, we investigate loop formation (47, 48) by means of PET-FCS measurements (49, 50). Specifically, we monitor static fluorescence quenching by the formation of a nonfluorescent complex between a fluorophore (here, Oxa11) and the quencher (Trp) (49, 50) in an 18-residue segment within protein L (*SI Appendix*, Table S1). This process results in an approximately exponential decay in the fluorescence correlation curve, where the corresponding

amplitude, c_q , and relaxation time, τ_q , are linked to the observed rate coefficients of forming and breaking the complex, k_+^{obs} and k_-^{obs} , respectively, by $\tau_q = 1/(k_+^{obs} + k_-^{obs})$ and $c_q = f_u k_+^{obs} / k_-^{obs}$, where f_u is the fraction of unfolded protein (50) (SI Appendix and SI Appendix, Fig. S3). To separate the contributions of k_+^{obs} and k_-^{obs} , it is thus necessary to quantify both c_q and τ_q , ideally under conditions where the protein is completely unfolded, so that f_u does not affect the amplitude. Here, we used a microfluidic mixing device that allows us to dilute the protein rapidly from fully denaturing (3 M GdmCl) to native conditions (0.3 M GdmCl) or intermediate GdmCl concentrations with millisecond dead time (51), enabling the observation of unfolded-state dynamics for all conditions before the protein folds. Measurements of the FRET-labeled protein in the microfluidic device confirmed that the protein was predominantly unfolded at times less than 5 ms after dilution of the denaturant (SI Appendix and SI Appendix, Fig. S4). The PET-FCS curves (Fig. 4B) exhibit a pronounced decay on the ~ 100 -ns time scale, which is absent in the control protein missing the Trp residue (SI Appendix, Fig. S5).

The diffusion-limited contact formation rate, k_+ , can be obtained by correcting the observed rate, k_+^{obs} , for the quenching efficiency, ϕ^* , which corresponds to the probability of forming the quenched state from the encounter complex (Fig. 4C, Inset and SI Appendix, Figs. S6 and S7). At denaturant concentrations approaching zero, we found a diffusion-limited contact formation time of $1/k_+ \approx 200$ ns. Notably, the formation of this contact is slower by a factor of ~ 10 (taking into account the contribution of tail effects and the difference in contact radii) compared with values reported for disordered peptides of similar length [Gly-Ser or Ala-Gly-Gln repeats (48, 52, 53)], already providing an indication for the presence of internal friction in unfolded protein L. With increasing denaturant concentration, $1/k_+$ decreases and approaches 100 ns at 3.5 M GdmCl (Fig. 4C). [We restricted our analysis of contact-based dynamics to below 3.5 M GdmCl, because above this concentration, the complex between Oxa11 and Trp is not sufficiently stable and, consequently, the amplitude from contact quenching becomes too small for a reliable analysis (SI Appendix and SI Appendix, Figs. S3 and S5).] This trend resembles the one observed for the reconfiguration time of the chain with FRET-FCS in the same denaturant range (Fig. 3C), but the contact formation time for this 18-residue segment is almost twofold greater than τ_r for the 57-residue segment. Can the contribution of internal friction identified in the FRET-FCS experiments explain the observed rate of loop formation?

Reconciling Reconfiguration Times and Contact Formation Times. Our FRET-FCS data (Fig. 3C) suggest that at low denaturant concentration (< 3 M GdmCl), unfolded protein L is well within the regime where internal friction dominates its global reconfiguration dynamics (i.e., $\tau_r \approx \tau_i$). When the solvent component, τ_s , is rescaled (12, 36, 54) from the 57-residue segment probed by FRET to the 18-residue segment length probed by PET, the relative contribution of τ_i becomes even more dominant because its absolute value is independent of segment length in the RIF model, accounting for more than 90% of the reconfiguration time of this segment. In this limit, the interresidue dynamics predicted by the RIF and ZIF models reduce to the simple diffusive case, and the contact formation time can be estimated using the Szabo-Schulten-Schulten (SSS) theory (55) in terms of 1D diffusion in a potential of mean force (36),

$$\tau_c^{IF} = \left(\frac{\pi}{6}\right)^{0.5} \frac{R_{47,64}}{R_c} \tau_i, \quad [2]$$

where $R_{47,64}$ is the RMS distance between the quencher and the dye at equilibrium, R_c is the effective contact radius at which quenching occurs, and τ_i at the respective GdmCl concentration is taken from the analysis of the FRET-FCS experiments (Fig. 3C). $R_{47,64}$ can be estimated by rescaling the mean square distance obtained from single-molecule FRET experiments assuming Gaussian chain statis-

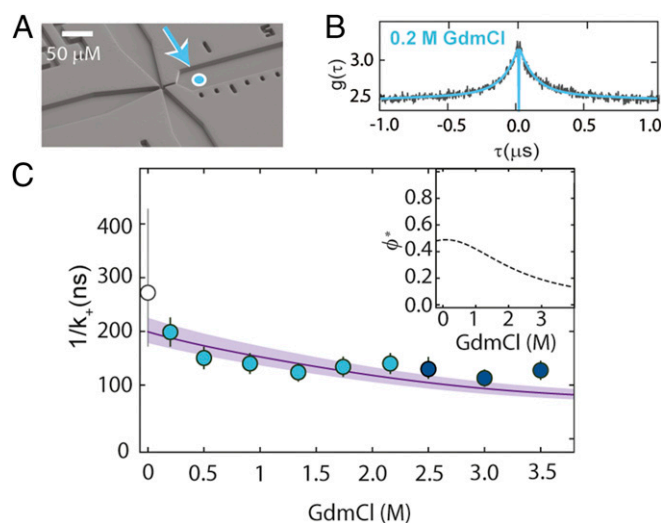


Fig. 4. Probing unfolded-state dynamics by PET. (A) Electron micrograph of the microfluidic mixing device (51) used for transiently populating unfolded protein L at low denaturant concentrations. Fully denatured protein in 3 M GdmCl in the sample inlet (left channel) is mixed with buffer from the side inlets (top and bottom channels) to measure the dynamics of the fully unfolded protein in the right observation channel at low denaturant concentrations. The cyan-filled circle identifies the first position where complete mixing is observed, corresponding to a time after mixing of ~ 4 ms. (B) PET-FCS measurement of unfolded protein L in 0.2 M GdmCl within the microfluidic device, with fit (blue line). (C) Contact formation time, obtained by correcting the observed rate, k_+^{obs} , for the GdmCl-dependent quenching efficiency, ϕ^* (Inset). The line shows the fit with Eq. 2. Error bars represent an average relative error of 13%, as estimated from the SD of multiple measurements at a single GdmCl concentration. The corresponding value of $1/k_+$ based on the MD simulation of unfolded protein L (31) with a contact radius of 0.83 ± 0.10 nm is shown as an empty circle with an error bar corresponding to a variation in the contact radius of 0.10 nm.

tics: The resulting value of $R_{47,64} = 2.4 \pm 0.2$ nm is in very good agreement with the one from the all-atom simulation, $R_{47,64}^{sim} = 2.3_{-0.3}^{+0.1}$ nm. The contact radius, R_c , depends on the specific properties of the dye-quencher pair and is used here as an adjustable parameter in the fit of the data.

Eq. 2 provides a remarkably good account of the experimental results (Fig. 4C), and the fit yields $R_c = 0.83 \pm 0.10$ nm, which is close to previous estimates ($R_c = 0.7 \pm 0.3$ nm) (45, 50, 56). Again, we can directly compare with the MD simulation: Using R_c from the fit of the experimental data, the contact formation time for the PET distance $R_{47,64}$ yields $\tau_c^{sim}(R_c = 0.83) = 270_{-100}^{+150}$ ns, in agreement with the measured data. [Here, the contact is estimated as occurring between the C^α atoms of W47 and G64. Contributions from the dye linker (that is not included in the simulation), the tryptophan side chain, and related local steric hindrance affect the value of R_c . Note, however, that for the contact times between the indole ring of W47 and the C^α of G64, steric hindrance effects are negligible for large contact radii ($R_c > 0.8$ nm) and become significant only for small values ($R_c \leq 0.6$ nm) (SI Appendix, Fig. S8).] Alternatively, we can estimate R_c by adjusting it to match the contact time from the MD simulations with the value measured at the lowest denaturant concentration, resulting in $R_c^{sim} = 0.9 \pm 0.2$ nm, again in the previously reported range (45, 50, 56). Interestingly, changing R_c from 1.0 nm [upper limit for the Oxa11-Trp pair (45)] to 0.4 nm [contact radius for the Trp-Cys pair (57)] in the analysis of the simulations leads to a roughly 100-fold increase in the relaxation time [$\tau_c^{sim}(R_c = 0.4 \text{ nm}) = 6.8 \mu\text{s}$]. This observation may explain, at least in part, the surprisingly slow decays previously reported for contact formation experiments in unfolded protein L ($\sim 5 \mu\text{s}$) based on Trp-Cys quenching (18, 30). Indeed, for the 10-residue segment studied by Waldauer et al. (18), the MD simulation (31) yields a diffusion-limited contact time for the indole ring of W47 and the C^α of T57 of 6.3 μs . The similarity of this time to the 6.8 μs

obtained from the simulations for the 17-residue segment probed in our PET experiments, despite the difference in sequence length, is at variance with the prediction for a simple polymer model (Eq. 2), and is likely to reflect the pronounced sensitivity of contact formation to the detailed properties of the chain, such as local structure formation or steric accessibility (53, 58) (*SI Appendix*, Figs. S2, S8, and S13). We also note that our results indicate a weaker viscosity dependence than the data of Waldauer et al. (18).

In summary, the contribution of internal friction obtained from the measurement of reconfiguration times based on FRET is in agreement with the contact formation experiments using PET, and both are in accord with the all-atom simulations. However, the strong sensitivity of contact formation experiments to R_c is an important factor to be taken into account.

Discussion

There is growing consensus regarding the importance of internal friction for the dynamics of unfolded proteins and peptides both from experiments and simulations (12, 19–21, 24, 59, 60), but apparent discrepancies in the time scales observed with different experimental methods have remained (12, 16, 18), raising the question of their consistency. Here, we used two complementary single-molecule techniques, FRET and PET, which are sensitive to distance changes on very different length scales: the former near the Förster radius ($\sim 5 \pm 3$ nm) and the latter in the sub-nanometer regime of contact formation (Fig. 1 *A* and *C*). This combination thus allows us to probe unfolded-state dynamics and the contribution of internal friction for different parts of the intramolecular distance distribution. By comparison with all-atom MD simulations and based on theoretical models that describe the contribution of internal friction either within the framework of Rouse/Zimm-type polymer dynamics or in terms of diffusion in a potential of mean force corresponding to the distance distribution (36, 55, 61), a coherent picture emerges from our results.

In the Rouse/Zimm picture of polymer dynamics, internal friction results in an additive component in the observed reconfiguration time (26, 36, 46), which we determined from FRET-FCS experiments (Fig. 3; Eq. 1). The internal friction time, τ_i , can then be incorporated in a simple model describing contact formation, the SSS approximation (55), in the limit of large internal friction (36). The resulting time scales for contact formation are in good agreement with our observations from the PET experiments (Fig. 4*C*). The consistency of the results based on the different experimental methods suggests that even though the two methods are sensitive to the dynamics on different length scales, simple models of polymer dynamics provide a unified description of these measurements and account for the diversity of the observed time scales.

We complement these results with a detailed analysis of a recent atomistic simulation of unfolded protein L. Availability of a long (86 μ s) simulated trajectory enables a detailed comparison of FRET with contact formation experiments, which requires sufficient sampling of infrequent contact formation events. The simulations agree well with the experimentally observed dimensions and dynamics of unfolded protein L (within 10%; Figs. 2–4), but do they show evidence for the presence of internal friction? Several observations suggest that this is indeed the case. The first indication comes from a comparison with other proteins for which simulations with the same force field and water model, as well as experimental data, are available. Prothymosin α (ProT α), for example, is a highly charged, and thus very expanded, intrinsically disordered protein (62) that exhibits very low internal friction, leading to an experimentally observed reconfiguration time of 45 ± 9 ns for the C56C110 segment (12) and 24 ± 4 ns for the C1C56 segment (63). The simulations of Piana et al. (31) recapitulate the expanded chain and its rapid dynamics, yielding a reconfiguration time for both segments of $\sim 27 \pm 20$ ns. In contrast, a more compact unfolded protein for which a similarly high contribution of internal friction as for protein L was observed is the cold shock protein (Csp) from *Thermotoga maritima*. Again, the relatively slow dynamics from experiment ($\tau_r = 116_{-40}^{+60}$ ns) (12, 16) and simulation ($\tau_r = 180_{-90}^{+70}$ ns) agree. The experimentally observed

correlation between compactness of unfolded proteins and the extent of internal friction (12) is thus also found in the simulations.

Even more revealing is the dependence of chain dynamics on the segment length of the chain. In the framework of the RIF and ZIF models, the absolute contribution of internal friction (τ_i) to the total reconfiguration time ($\tau_{m,n}$) is independent of the length, $|m-n|$, of the chain segment probed, whereas the solvent-dominated contribution (τ_s) decreases with decreasing chain length (12, 36). As a result, the relative contribution of τ_i increases for shorter segments, and internal friction can thus be quantified from the segment length dependence of chain relaxation, which has previously been used in experiments and simulations (12, 21). Fig. 5 illustrates this behavior for the MD simulations of protein L, Csp, and ProT α : Whereas $\tau_{m,n}$ remains high for all segment lengths in unfolded protein L and Csp, indicating a large contribution of internal friction, $\tau_{m,n}$ exhibits a steady decrease with decreasing segment length in ProT α , consistent with the prediction for a chain with very low internal friction (12, 21). The behavior observed in the simulations resembles the predictions of the RIF model with a large contribution of τ_i for unfolded protein L and Csp and the prediction of the Rouse model without internal friction for ProT α (Fig. 5), further supporting a pronounced difference in internal friction in the simulations.

Finally, given this consistency of experiments and simulations, what can we deduce about the molecular origin of internal friction? Persistent secondary structure and tertiary contacts are virtually absent in the simulations of all three proteins (~ 3 –4%) (*SI Appendix*, Fig. S9). This finding is in agreement with the low secondary structure content of unfolded Csp under native conditions, as determined by kinetic synchrotron radiation circular dichroism experiments (43), and suggests that native-like structural elements are not required for internal friction. Short-range nonnative hydrogen bonds (sequence separation less than six residues) are similarly prevalent in all three simulations (*SI Appendix*, Fig. S10), and are thus also unlikely to make a large contribution. However, protein L and Csp clearly differ from ProT α in their greater abundance of transient nonnative sequence-distant hydrogen bonds, salt bridges, and hydrophobic contacts (*SI Appendix*, Figs. S10–S12), which is not unexpected in view of the pronounced

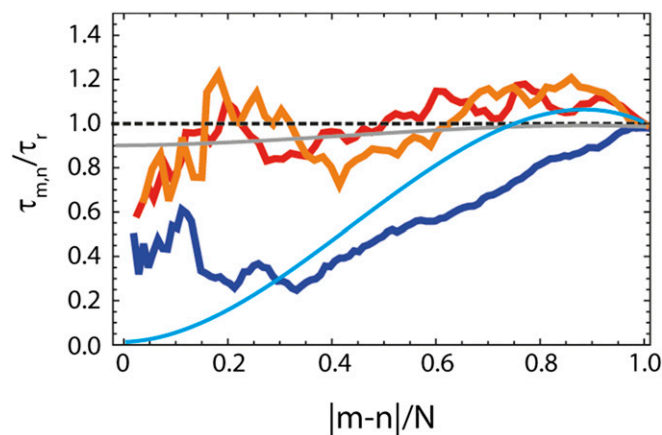


Fig. 5. Dependence of the relative reconfiguration time, $\tau_{m,n}/\tau_r$, on the relative length of the chain segment, $|m-n|/N$, based on the MD simulations (31) of unfolded protein L (orange), Csp (red), and ProT α (blue). The segment length, $|m-n|$, (where n is either 1 or N) and the reconfiguration time, $\tau_{m,n}$, (averaged between the two segments of equal lengths; details are provided in *SI Appendix*) are normalized by the total number of amino acids, N , or for the end-to-end reconfiguration time, τ_r , of the particular protein, respectively. The gray line shows the prediction of the RIF model with the value of τ_i from nsFCS measurements of unfolded protein L extrapolated to zero denaturant (Fig. 2). For comparison, the two extreme cases of the RIF model are also shown: the Rouse chain without internal friction (cyan line) and the limit of infinite internal friction (dashed black line).

differences in chain expansion observed in both simulations (31, 64) and experiments (12, 62) (Fig. 2). The correlation between chain dimensions, intrachain interactions, and internal friction observed in the simulations implies that intrachain interactions could also be the missing link for the experimentally observed correlation between unfolded-state compaction and internal friction (12, 23). To investigate this hypothesis further, we now turn to protein dynamics as revealed by the simulations.

Interestingly, for each of the three proteins, the respective average relaxation times are comparable for forming and breaking sequence-distant hydrogen bonds, salt bridges, and hydrophobic contacts; for dihedral angle rotations; and for the reconfiguration of short segments of approximately five residues (*SI Appendix, Figs. S11–S13*). This observation supports a coupling between intrachain interactions and dihedral angle rotations, which are required for large conformational rearrangements of the chain and have been implicated in internal friction based on previous simulations (20, 21, 26). However, there are marked differences between the behavior of the unfolded proteins with high and low internal friction, respectively: For unfolded protein L and Csp, all relaxation times are in the range of about 100–200 ns; for ProTx, they are almost an order of magnitude shorter, matching the difference in global chain reconfiguration times. The much faster dihedral hopping in ProTx (*SI Appendix, Fig. S13*) would imply that dihedral relaxation, per se, is not the dominant source of internal friction (20) but that interactions within the chain impede dihedral transitions. This conclusion is supported by the absence of internal friction in some unfolded proteins at high concentrations of denaturant (12) (at least to within experimental uncertainty), where intrachain interactions are weakened but dihedral barriers are not expected to be much different. However, even in the presence of nonnative interactions, relaxation dynamics in the vicinity of glycine residues are accelerated (*SI Appendix, Fig. S13*), and lowering the dihedral barriers in a compact unfolded state was found to reduce internal friction (21). It is tempting to identify the nonnative interactions between sequence-distant segments of the chain as leading to Cerf-type friction [as proposed by de Gennes (65)], as opposed to the Kuhn-type friction that results from crossing dihedral barriers (46, 65), but the coupling between dihedral dynamics and nonnative interactions suggests that the two mechanisms may not be separable. Future simulations and experiments addressing the length scaling of internal friction and the dependence of the two contributions on chain compaction may help to address this question in more detail.

How does the origin of internal friction suggested here differ from mechanisms proposed for transition states of folded proteins? As a protein approaches its native state, the influence of nonnative interactions is expected to decrease. Interestingly, however, an important contribution of nonnative salt bridges to internal friction has been identified in the folding transition state

of a designed protein (14), which may resemble the charge interactions in unfolded protein L and Csp (*SI Appendix, Fig. S11*). Dihedral rearrangements have been implicated as a mechanism of internal friction in protein folding, especially for helical proteins, where such local transitions are particularly important for the dynamics in the transition-state region (24, 25). A lack of solvent relaxation on the time scale of dihedral barrier crossing can also result in low sensitivity of dynamics to solvent viscosity, and thus contribute to the signature commonly ascribed to internal friction (20, 25). For a fully folded protein, most of the protein atoms are excluded from the solvent, and internal friction can be assumed to result from collisions with other protein atoms instead of solvent molecules (9). The relative contributions of different interactions and mechanisms to internal friction are thus likely to depend on the progress of the folding reaction and the proximity to the native state.

In summary, the combination of two complementary single-molecule techniques with atomistic simulations provides a consistent picture of protein dynamics in the unfolded state, reveals a significant contribution of internal friction, and quantifies its magnitude. The results not only reconcile the different time scales observed in FRET and contact formation experiments but also illustrate that the recent advances in force field development now enable more realistic simulations of unfolded and intrinsically disordered proteins, in terms of both chain dimensions and dynamics. Notably, the results based on simple polymer models for the distance distributions and dynamics in the unfolded state agree well with the results using the distributions from recent all-atom simulations, supporting the use of simple models for the analysis of experimental and simulation data. The close integration of multiple experimental techniques with theory and simulations used here overcomes limitations of each individual approach. The increasing convergence of time scales in experiments and simulations and the continued improvements in force fields benchmarked with experimental data will enable an increasingly reliable interpretation of experimental observables based on molecular simulations. This synergy is an important step toward quantifying the molecular contributions to internal friction and the resulting influence on processes such as interactions of intrinsically disordered proteins and protein folding dynamics.

ACKNOWLEDGMENTS. We thank D. E. Shaw Research, especially Stefano Piana-Agostinetti and Rebecca Bish-Cornelissen, for providing access to their MD trajectories. We thank Amedeo Caflich, Andreas Vitalis, and Marco Bacci for assistance in the trajectory analysis with CAMPARI. We thank Robert Best, Alessandro Borgia, Hagen Hofmann, Kresten Lindorff-Larsen, Hannes Neuweiler, Stefano Piana, Markus Sauer, and Attila Szabo for helpful discussions and comments on the manuscript. This work was supported by the Swiss National Science Foundation and a Starting Investigator Grant of the European Research Council (to B.S.). D.E.M. acknowledges support from the Robert A. Welch Foundation and the US National Science Foundation.

1. Bryngelson JD, Onuchic JN, Socci ND, Wolynes PG (1995) Funnels, pathways, and the energy landscape of protein folding: A synthesis. *Proteins* 21(3):167–195.
2. Dill KA, Chan HS (1997) From Levinthal to pathways to funnels. *Nat Struct Biol* 4(1):10–19.
3. Camacho CJ, Thirumalai D (1993) Kinetics and thermodynamics of folding in model proteins. *Proc Natl Acad Sci USA* 90(13):6369–6372.
4. Hänggi P, Talkner P, Borkovec M (1990) Reaction-rate theory: 50 years after Kramers. *Rev Mod Phys* 62:251–341.
5. Pabit SA, Roder H, Hagen SJ (2004) Internal friction controls the speed of protein folding from a compact configuration. *Biochemistry* 43(39):12532–12538.
6. Cellmer T, Henry ER, Hofrichter J, Eaton WA (2008) Measuring internal friction of an ultrafast-folding protein. *Proc Natl Acad Sci USA* 105(47):18320–18325.
7. Plaxco KW, Baker D (1998) Limited internal friction in the rate-limiting step of a two-state protein folding reaction. *Proc Natl Acad Sci USA* 95(23):13591–13596.
8. Qiu LL, Hagen SJ (2004) Internal friction in the ultrafast folding of the tryptophan cage. *Chem Phys* 307:243–249.
9. Ansari A, Jones CM, Henry ER, Hofrichter J, Eaton WA (1992) The role of solvent viscosity in the dynamics of protein conformational changes. *Science* 256(5065):1796–1798.
10. Borgia A, et al. (2012) Localizing internal friction along the reaction coordinate of protein folding by combining ensemble and single-molecule fluorescence spectroscopy. *Nat Commun* 3:1195.
11. Wensley BG, et al. (2010) Experimental evidence for a frustrated energy landscape in a three-helix-bundle protein family. *Nature* 463(7281):685–688.
12. Soranno A, et al. (2012) Quantifying internal friction in unfolded and intrinsically disordered proteins with single-molecule spectroscopy. *Proc Natl Acad Sci USA* 109(44):17800–17806.
13. Hagen SJ (2010) Solvent viscosity and friction in protein folding dynamics. *Curr Protein Pept Sci* 11(5):385–395.
14. Chung HS, Piana-Agostinetti S, Shaw DE, Eaton WA (2015) Structural origin of slow diffusion in protein folding. *Science* 349(6255):1504–1510.
15. Frauenfelder H, Wolynes PG (1985) Rate theories and puzzles of hemeprotein kinetics. *Science* 229(4711):337–345.
16. Nettels D, Gopich IV, Hoffmann A, Schuler B (2007) Ultrafast dynamics of protein collapse from single-molecule photon statistics. *Proc Natl Acad Sci USA* 104(8):2655–2660.
17. Neuweiler H, Johnson CM, Fersht AR (2009) Direct observation of ultrafast folding and denatured state dynamics in single protein molecules. *Proc Natl Acad Sci USA* 106(44):18569–18574.
18. Waldauer SA, Bakajin O, Lapidus LJ (2010) Extremely slow intramolecular diffusion in unfolded protein L. *Proc Natl Acad Sci USA* 107(31):13713–13717.
19. Schulz JCF, Schmidt L, Best RB, Dzubiella J, Netz RR (2012) Peptide chain dynamics in light and heavy water: Zooming in on internal friction. *J Am Chem Soc* 134(14):6273–6279.
20. de Sancho D, Sirur A, Best RB (2014) Molecular origins of internal friction effects on protein-folding rates. *Nat Commun* 5:4307.
21. Echeverria I, Makarov DE, Papoian GA (2014) Concerted dihedral rotations give rise to internal friction in unfolded proteins. *J Am Chem Soc* 136(24):8708–8713.

22. Sizemore SM, Cope SM, Roy A, Ghirlanda G, Vaiana SM (2015) Slow internal dynamics and charge expansion in the disordered protein CGRP: A comparison with amylin. *Biophys J* 109(5):1038–1048.
23. Schuler B, Soranno A, Hofmann H, Nettels D (2016) Single-molecule FRET spectroscopy and the polymer physics of unfolded and intrinsically disordered proteins. *Annu Rev Biophys* 45:207–231.
24. Zheng W, De Sancho D, Hoppe T, Best RB (2015) Dependence of internal friction on folding mechanism. *J Am Chem Soc* 137(9):3283–3290.
25. Zheng W, de Sancho D, Best RB (2016) Modulation of folding internal friction by local and global barrier heights. *J Phys Chem Lett* 7(6):1028–1034.
26. Portman JJ, Takada S, Wolynes PG (2001) Microscopic theory of protein folding rates. II. Local reaction coordinates and chain dynamics. *J Chem Phys* 114:5082–5096.
27. Hofmann H, et al. (2014) Role of denatured-state properties in chaperonin action probed by single-molecule spectroscopy. *Biophys J* 107(12):2891–2902.
28. Zerze GH, Mittal J, Best RB (2016) Diffusive dynamics of contact formation in disordered polypeptides. *Phys Rev Lett* 116(6):068102.
29. Shaw DE, et al. (2009) Millisecond-scale molecular dynamics simulations on Anton. *Proceedings of the Conference on High Performance Computing Networking, Storage and Analysis* (Association for Computing Machinery, New York).
30. Voelz VA, Singh VR, Wedemeyer WJ, Lapidus LJ, Pande VS (2010) Unfolded-state dynamics and structure of protein L characterized by simulation and experiment. *J Am Chem Soc* 132(13):4702–4709.
31. Piana S, Donchev AG, Robustelli P, Shaw DE (2015) Water dispersion interactions strongly influence simulated structural properties of disordered protein states. *J Phys Chem B* 119(16):5113–5123.
32. Best RB, Zheng W, Mittal J (2014) Balanced protein-water interactions improve properties of disordered proteins and non-specific protein association. *J Chem Theory Comput* 10(11):5113–5124.
33. Vitalis A, Pappu RV (2009) ABSINTH: A new continuum solvation model for simulations of polypeptides in aqueous solutions. *J Comput Chem* 30(5):673–699.
34. Nerenberg PS, Jo B, So C, Tripathy A, Head-Gordon T (2012) Optimizing solute-water van der Waals interactions to reproduce solvation free energies. *J Phys Chem B* 116(15):4524–4534.
35. Huang J, et al. (2017) CHARMM36m: An improved force field for folded and intrinsically disordered proteins. *Nat Methods* 14(1):71–73.
36. Cheng RR, Hawk AT, Makarov DE (2013) Exploring the role of internal friction in the dynamics of unfolded proteins using simple polymer models. *J Chem Phys* 138(7):074112.
37. Sherman E, Haran G (2006) Coil-globule transition in the denatured state of a small protein. *Proc Natl Acad Sci USA* 103(31):11539–11543.
38. Merchant KA, Best RB, Louis JM, Gopich IV, Eaton WA (2007) Characterizing the unfolded states of proteins using single-molecule FRET spectroscopy and molecular simulations. *Proc Natl Acad Sci USA* 104(5):1528–1533.
39. Voelz VA, et al. (2012) Slow unfolded-state structuring in Acyl-CoA binding protein folding revealed by simulation and experiment. *J Am Chem Soc* 134(30):12565–12577.
40. Haran G (2012) How, when and why proteins collapse: The relation to folding. *Curr Opin Struct Biol* 22(1):14–20.
41. Borgia A, et al. (2016) Consistent view of polypeptide chain expansion in chemical denaturants from multiple experimental methods. *J Am Chem Soc* 138(36):11714–11726.
42. Schuler B, Lipman EA, Eaton WA (2002) Probing the free-energy surface for protein folding with single-molecule fluorescence spectroscopy. *Nature* 419(6908):743–747.
43. Hoffmann A, et al. (2007) Mapping protein collapse with single-molecule fluorescence and kinetic synchrotron radiation circular dichroism spectroscopy. *Proc Natl Acad Sci USA* 104(1):105–110.
44. Case DA, et al. (2012) AMBER 12 (University of California, San Francisco).
45. Doose S, Neuweiler H, Sauer M (2009) Fluorescence quenching by photoinduced electron transfer: A reporter for conformational dynamics of macromolecules. *Chemphyschem* 10:1389–1398.
46. Khatri BS, McLeish TCB (2007) Rouse model with internal friction: A coarse grained framework for single biopolymer dynamics. *Macromolecules* 40:6770–6777.
47. Hagen SJ, Hofrichter J, Szabo A, Eaton WA (1996) Diffusion-limited contact formation in unfolded cytochrome c: Estimating the maximum rate of protein folding. *Proc Natl Acad Sci USA* 93(21):11615–11617.
48. Krieger F, Fierz B, Bieri O, Drewello M, Kiefhaber T (2003) Dynamics of unfolded polypeptide chains as model for the earliest steps in protein folding. *J Mol Biol* 332(1):265–274.
49. Neuweiler H, Schulz A, Böhmer M, Enderlein J, Sauer M (2003) Measurement of submicrosecond intramolecular contact formation in peptides at the single-molecule level. *J Am Chem Soc* 125(18):5324–5330.
50. Doose S, Neuweiler H, Sauer M (2005) A close look at fluorescence quenching of organic dyes by tryptophan. *Chemphyschem* 6:2277–2285.
51. Wunderlich B, et al. (2013) Microfluidic mixer designed for performing single-molecule kinetics with confocal detection on timescales from milliseconds to minutes. *Nat Protoc* 8(8):1459–1474.
52. Neuweiler H, Löllmann M, Doose S, Sauer M (2007) Dynamics of unfolded polypeptide chains in crowded environment studied by fluorescence correlation spectroscopy. *J Mol Biol* 365(3):856–869.
53. Buscaglia M, Lapidus LJ, Eaton WA, Hofrichter J (2006) Effects of denaturants on the dynamics of loop formation in polypeptides. *Biophys J* 91(1):276–288.
54. Makarov DE (2010) Spatiotemporal correlations in denatured proteins: The dependence of fluorescence resonance energy transfer (FRET)-derived protein re-configuration times on the location of the FRET probes. *J Chem Phys* 132(3):035104.
55. Szabo A, Schulten K, Schulten Z (1980) First passage time approach to diffusion controlled reactions. *J Chem Phys* 72:4350–4357.
56. Vaiana AC, et al. (2003) Fluorescence quenching of dyes by tryptophan: Interactions at atomic detail from combination of experiment and computer simulation. *J Am Chem Soc* 125(47):14564–14572.
57. Lapidus LJ, Eaton WA, Hofrichter J (2001) Dynamics of intramolecular contact formation in polypeptides: Distance dependence of quenching rates in a room-temperature glass. *Phys Rev Lett* 87(25):258101.
58. Toan NM, Morrison G, Hyeon C, Thirumalai D (2008) Kinetics of loop formation in polymer chains. *J Phys Chem B* 112(19):6094–6106.
59. Alexander-Katz A, Wada H, Netz RR (2009) Internal friction and nonequilibrium unfolding of polymeric globules. *Phys Rev Lett* 103(2):028102.
60. Schulz JCF, Miettinen MS, Netz RR (2015) Unfolding and folding internal friction of β -hairpins is smaller than that of α -helices. *J Phys Chem B* 119(13):4565–4574.
61. Gopich IV, Nettels D, Schuler B, Szabo A (2009) Protein dynamics from single-molecule fluorescence intensity correlation functions. *J Chem Phys* 131(9):095102.
62. Müller-Spätth S, et al. (2010) From the Cover: Charge interactions can dominate the dimensions of intrinsically disordered proteins. *Proc Natl Acad Sci USA* 107(33):14609–14614.
63. König I, et al. (2015) Single-molecule spectroscopy of protein conformational dynamics in live eukaryotic cells. *Nat Methods* 12(8):773–779.
64. Wuttke R, et al. (2014) Temperature-dependent solvation modulates the dimensions of disordered proteins. *Proc Natl Acad Sci USA* 111(14):5213–5218.
65. de Gennes PG (1979) *Scaling Concepts in Polymer Physics* (Cornell Univ Press, Ithaca, NY).

Supporting Information

Material and Methods

Protein preparation and labeling. A pET47b(+)-based plasmid for the expression of the protein L FRET mutant (C7-C64) with an N-terminal His₆-tag and a subsequent recognition site for HRV 3C protease was obtained from Celtek Genes (Franklin, USA). Two more protein L variants, the protein L PET mutant (C64) and control mutant (F47-C64) were generated using site-directed mutagenesis. All three variants were expressed recombinantly in *E. coli* BL21(DE3). 2 L cultures were grown in LB medium to OD₆₀₀ ≈ 0.8 and then induced with 1 mM IPTG for 4 hours at 37°C. After harvesting by centrifugation, the cells were resuspended in Lysis Buffer (100 mM NaH₂PO₄ and 10 mM Tris, 6 M GdmCl, 10 mM imidazole, pH 8). His₆-tagged protein L was purified from the soluble fraction of the lysate using Ni Sepharose (GE Healthcare Bio-Sciences AB, Uppsala, Sweden). Bound protein was eluted with a gradient of 10 to 170 mM imidazole in Lysis Buffer. The pooled fractions containing protein L were subjected to one-step refolding and cleavage of the His₆-tag. Refolding of protein L was achieved by dialysis against Cleavage Buffer (100 mM NaH₂PO₄, 100 mM NaCl, 1 mM DTT, pH 7.4) after adding HRV 3C Protease (produced in-house) at a protein-to-protease molar ratio of about 100 to 1. The cleavage reaction was stopped by adding GdmCl to a final concentration of 4.8 M. The His₆-tag containing peptide and uncleaved protein were separated from protein L using a 5 ml HisTrap column (GE Healthcare Bio-Sciences AB, Uppsala, Sweden). Protein L in the flow-through fractions was reduced with 50 mM DTT, concentrated and subjected to gel filtration using a Superdex 75 10/300 GL column (GE Healthcare Bio-Sciences AB, Uppsala, Sweden) in 100 mM NaH₂PO₄, 6 M GdmCl, pH 7.1. The protein L FRET variant was labeled with Alexa Fluor 488 maleimide (Molecular Probes, Eugene, USA) at a dye/protein molar ratio of 0.7/1 for 2 h at room temperature, and subsequently with Alexa Fluor 594 maleimide at a dye/protein molar ratio of 2/1 over night at 4 °C. The protein L PET variants were labeled with ATTO-Oxa11 maleimide (ATTO-TEC GmbH, Siegen, Germany) at a dye/protein molar ratio of 3/1 for 3 h at room temperature. Unreacted dyes were removed by gel filtration using a Superdex 75 10/300 GL column (GE Healthcare Bio-Sciences AB, Uppsala, Sweden) in 100 mM NaH₂PO₄, 6 M GdmCl, pH 7.1. The correct molecular mass of all labeled protein samples was verified by electrospray ionization mass spectrometry.

Single-molecule fluorescence spectroscopy. Single-molecule fluorescence measurements were performed with a MicroTime 200 confocal microscope (PicoQuant, Germany) equipped with an Olympus UplanApo 60x/1.20W objective (Olympus). For single-molecule FRET measurements, a diode laser (LDH-D-C-485, PicoQuant, Germany) was synchronized with a 20 MHz supercontinuum laser (SC-450-4, Fianium, UK) filtered by a z582/15 band pass filter (Chroma) for pulsed interleaved excitation (PIE) (66) of labeled molecules. For FRET-FCS measurements, the same diode laser was used in continuous-wave mode to excite the donor dye. Photons emitted from the sample were collected by the objective, and scattered light was suppressed by a filter (HQ500LP, Chroma Technology) before the emitted photons passed the confocal pinhole (100 μm diameter). The emitted photons were then distributed into four channels, first by a polarizing beam splitter and then by a dichroic mirror (585DCXR, Chroma) for each polarization. Donor and acceptor emission was filtered (ET525/50m or HQ650/100m, respectively, Chroma Technology) and then focused on a τ-SPAD avalanche photodiode (PicoQuant). The arrival time of every detected photon was recorded with a HydraHarp 400 counting module (PicoQuant). For PET-FCS measurements, a Helium Neon laser at 632.8 nm (05-LHP-925, Melles Griot) was employed to excite ATTO-Oxa11. The collected photons were separated into two channels by a polarizing beam splitter (zt 633 RDC, Chroma), filtered with

a band pass filter (ET685/50, Chroma) and an IR-filter (HC 720/SP, Semrock), and detected by τ -SPAD avalanche photodiodes (PicoQuant). All experiments were performed on molecules freely diffusing in solution.

FRET experiments were performed by exciting the donor dye with a laser power of 100 μ W (measured at the back aperture of the objective). For pulsed interleaved excitation (66) of donor and acceptor, the power used for exciting the acceptor dye was adjusted to match the acceptor emission intensity to that of the donor (between 50 and 70 μ W). Single-molecule FRET efficiency histograms were acquired from samples with protein concentrations between 50 pM and 100 pM. Trigger times for excitation pulses (repetition rate 20 MHz) and photon detection events were stored with 16 ps resolution.

For FRET-FCS, samples of labeled protein with a concentration of 1 nM were excited by the diode laser in continuous-wave mode at 100 μ W. All measurements were performed in 50 mM sodium phosphate buffer, pH 7.0, 143 mM 2-mercaptoethanol (for photoprotection), 0.001% Tween 20 (for surface passivation) and GdmCl at the reported concentrations. Note that the FRET-FCS experiments reported here (i.e. above 0.5 M GdmCl) exhibit the pronounced anticorrelated component in the donor-acceptor crosscorrelation characteristic of donor-acceptor distance fluctuations, indicating that other contributions to the correlation function, such as PET quenching of the Alexa dyes, are negligible, as expected for this sequence separation (67).

Microfluidic mixing experiments. Microfluidic devices were fabricated using replica molding in poly(dimethylsiloxane) (PDMS) as described previously (51). The microfluidic device was mounted in a custom-made holder that allows the pressure driving the flow to be regulated individually for each channel. In the experiment (see Fig. 4A), we applied 13.8 kPa to the center inlet and 13.8 kPa to the side inlets, resulting in rapid dilution of the protein in high denaturant entering from the central inlet channel with buffer from the side inlet channels at a mixing ratio of 1:10. We acquired data at a position after the mixing region corresponding to 4 ms after mixing.

Ensemble time-correlated single-photon counting. High-resolution fluorescence lifetime decays were acquired with a custom-built instrument (68) in magic-angle configuration (69), using a supercontinuum laser source (SC-450-4, 20 MHz, Fianium, Southampton, U.K.) for excitation, resulting in a width of 80 ps for the instrument response function (full width at half-maximal intensity). Bimolecular quenching experiments were performed in 100 mM sodium phosphate buffer (pH 7.2) with 143 mM 2-mercaptoethanol, 0.001% (v/v) Tween 20, 25 nM of Atto-Oxa11, and the concentrations of tryptophan, GdmCl, and glycerol as specified.

Data Analysis

FRET efficiency and fluorescence lifetime histograms. Fluorescence bursts from individual molecules were identified by combining successive photons separated by inter-photon times of less than 150 μ s and retaining the burst only if the total number of photons detected after donor excitation was greater than 50. Transfer efficiencies for each burst were calculated according to $E = n_A / (n_A + n_D)$, where n_D and n_A are the numbers of donor and acceptor photons, respectively, corrected for background, acceptor direct excitation, channel crosstalk, differences in detector efficiencies, and quantum yields of the dyes (70). The precision of the measured transfer efficiencies as estimated from multiple independent measurements is typically ± 0.02 transfer efficiency units and thus comparable to or smaller than the data points reported in the figures, unless error bars are shown explicitly. Changes in refractive index caused by denaturant were

measured with a digital Abbe refractometer (Krüss, Germany) and were used to correct the Förster radius (R_0) for each sample.

Multiparameter detection allows us to exclude possible interfering artifacts, such as insufficient rotational averaging of the fluorophores or quenching of the dyes (71). The dependence of the fluorescence lifetimes on transfer efficiencies determined for each burst was compared with the behavior expected for fixed distances and for a chain sampling a broad distribution of distances. For a fixed distance, r , the mean donor lifetime in the presence of acceptor is given by $\tau_{DA}(r) = \tau_D (1-E(r))$, where τ_D is the donor lifetime in the absence of the acceptor, and $E(r) = 1/(1+r^6/R_0^6)$. For a dynamic chain with a dye-to-dye distance distribution, $P(r)$, the average donor lifetime is $\tau_{DA} = \int_0^\infty t I(t) dt / \int_0^\infty I(t) dt$ with $I(t) = I_0 \int_0^\infty P(r) e^{-t/\tau_{DA}(r)} dr$, where $I(t)$ is the time-resolved fluorescence emission intensity following donor excitation. Subpopulation-specific anisotropies were determined for both donor and acceptor, and values were found to vary between 0.23 and 0.19 for the donor and between 0.11 and 0.09 for the acceptor, consistent with values observed in ensemble measurements, and sufficiently low to assume as a good approximation for the orientational factor $\kappa^2 = 2/3$.

Quantifying distances from transfer efficiencies. Histograms of transfer efficiencies were fitted with three empirical peak functions, using a normal distribution for the donor-only and unfolded populations; the folded state was fitted to a log-normal distribution to account for the asymmetry of peaks at high transfer efficiency. Mean values of transfer efficiency, $\langle E \rangle$, corresponding to the unfolded population, were related to distance information by solving numerically

$$\langle E \rangle = \int E(r)P(r)dr, \quad (\text{Eq. S1})$$

where $P(r)$ is the distance distribution of an appropriate polymer model that accounts for the intramolecular distances sampled by the chain. We used three different distributions:

- the random walk (Gaussian) chain:

$$P_{Gauss}(r) = 4\pi r^2 \left(\frac{3}{2\pi R^2} \right)^{3/2} \exp\left(-\frac{3r^2}{2R^2} \right), \quad (\text{Eq. S2})$$

where R is the root-mean-square value of the interdye distance;

- the self-avoiding-walk (SAW):

$$P_{SAW}(r) = 4\pi r^2 \frac{0.278}{R^3} \left(\frac{r}{R} \right)^{0.28} \exp\left(-1.206 \left(\frac{r}{R} \right)^{2.43} \right), \quad (\text{Eq. S3})$$

- and the Worm-like chain:

$$P_{WLC}(r) = Z \frac{4\pi (r/l_c)^2}{l_c [1 - (r/l_c)^2]^{9/2}} \exp\left(\frac{-3l_c}{4l_p (1 - (r/l_c)^2)} \right), \quad (\text{Eq. S4})$$

where Z is a normalization factor, l_c is the contour length, and l_p the persistence length of the chain. Eq. S1 was then solved either for R or l_p .

Finally, to account for the length of dye linkers and compare the experimental data with simulations, the root-mean-squared interdye distance R was rescaled according to $R_{m,n} = |m-n|^{0.5}/|m-n+2l|^{0.5}$ with $l = 4.5$ (43, 72). The same scaling law was used to estimate the intra-chain root-mean-square distance for the PET construct, $R_{47,64} = R_{7,64} (64-47)^{0.5}/(64-7)^{0.5}$. It is interesting to compare the polymer models with the corresponding distance distributions from the MD simulation. In Fig. 2, although the variances of the distributions may differ by up to 30%, the ratio of the second moments from the polymer model and MD distributions are 1.01 for the GC and WLC and 0.96 for the SAW, whereas the ratio of the fourth moments is 0.86 for the GC, 0.83 for the WLC, and 0.78 for the SAW. Overall, simple polymer models capture the global properties of the internal distances sampled in the MD simulations well (see Fig. S1) but can of course not describe deviations due to specific local structure formation that can occur in atomistic models.

Reconfiguration times from FRET-FCS

Autocorrelation curves of acceptor and donor channels and cross-correlation curves between acceptor and donor channels were computed from the measurements and analyzed as described previously (10, 12, 61). The data were fitted over a time window of 4 μ s according to

$$g_{ij}(\tau) = 1 + \frac{1}{N} (1 - c_{AB} e^{-\frac{\tau-t_0}{\tau_{AB}}}) (1 + c_{CD} e^{-\frac{\tau-t_0}{\tau_b}}) (1 + c_T e^{-\frac{\tau-t_0}{\tau_T}}), \quad i, j = A, D \quad (S5)$$

where N is the mean number of molecules in the confocal volume, c_{AB} , c_{CD} , c_T are the amplitudes related to photon antibunching (AB), chain dynamics (CD), and triplet blinking of the dyes (T), and τ_{AB} , τ_{CD} , τ_T are the corresponding relaxation times. Assuming that chain dynamics can be described as a diffusive process in the potential of mean force derived from the sampled distance distribution $P(r)$ (16), we convert τ_{CD} to the reconfiguration time of the chain, τ_r (61). Since atomistic simulations are available only in the absence of denaturant, we employ the Gaussian chain model to obtain suitable distance distributions for all GdmCl concentrations investigated. Note that τ_{CD} and τ_r differ by only 5 to 10 % in the present case because the average distance is close to the Förster radius under all conditions (61). The analysis of FRET-FCS measurements was restricted to above 0.5 M GdmCl because of a static quenching component that becomes detectable at lower denaturant concentrations, as indicated by a correlated amplitude of the donor-acceptor crosscorrelation observed in microfluidic mixing experiments.

Separating internal friction and solvent components of the reconfiguration time.

According to the Rouse and Zimm model with internal friction (12, 36, 46), the reconfiguration time of the chain can be described as a sum of two components, τ_s and τ_r (see Eq. 1). To separate these two components, we adopted the following procedure. First, we studied the solvent viscosity dependence of τ_r at 6M GdmCl (Fig 3C, inset, purple). By linear extrapolation of τ_r to $\eta_s = 0$, we identified a considerable contribution of internal friction even at this high denaturant concentration, corresponding to $\tau_r(6 \text{ M}) \approx 28 \pm 5$ ns and $\tau_s(6 \text{ M}) \approx 35 \pm 7$ ns, similar in magnitude to the spectrin domains (10) and ubiquitin (72) under similar conditions. To quantify τ_s over the entire denaturant range, we rescaled $\tau_s(6\text{M})$ by the values of $R^2 \eta_s$ corresponding to each GdmCl concentration (10, 12) (Fig. 3C, blue line). Finally, to obtain an estimate of the internal friction contribution for all denaturant concentrations, we subtracted the rescaled τ_s from a polynomial interpolation of the measured reconfiguration times (Fig. 3C, orange line). We optimize the estimate by allowing the solvent and internal friction components in the model to be adjusted within the bounds of the propagated experimental errors and assuming that the internal friction remains constant above 6M GdmCl. As a consistency check, we studied the

viscosity dependence at 2M GdmCl (Fig 3C, inset, magenta). We found $\tau_i(2\text{ M}) \approx 40 \pm 10$ ns and $\tau_s(2\text{ M}) \approx 10 \pm 5$ ns, in line with the predictions from the Rouse model (see Fig. 3C).

Bimolecular dynamic quenching of Trp and ATTO Oxa11 from fluorescence lifetimes. The recorded fluorescence lifetime decays were fitted with single-exponential decays convolved with the instrument response function (IRF) obtained from the measurement of scattered laser light (50). The buffer contained 100 mM potassium phosphate pH 7.2, 143 mM 2-mercaptoethanol, and 0.001% Tween 20. A dye concentration of 25 nM was used for Oxa11.

PET-FCS measurements of bimolecular quenching between Trp and ATTO Oxa11. The static quenching rate of Oxa11 by Trp was obtained via bimolecular PET-FCS measurements of Oxa11 in the presence of a fixed concentration of Trp at varying GdmCl concentration. The dynamic quenching rate was obtained from the change in fluorescence lifetime of Oxa11 in the presence and absence of Trp at different concentrations of GdmCl, as reported in Fig. S6A. The fluorescence lifetime of Oxa11, τ_{Oxa11} , at a given Trp concentration, c_{Trp} , is related to the dynamic quenching rate via $k_{\text{coll}}^{\text{dyn}} = 1/\tau_{\text{Oxa11}}(c_{\text{Trp}}) - 1/\tau_{\text{Oxa11}}(0)$. A theoretical estimate of the bimolecular collision rate can be obtained from the Smoluchowski theory for diffusion-limited reactions:

$$k_{\text{coll}}^{\text{theo}} = 4\pi N_A (D_{\text{Trp}} + D_{\text{Oxa11}})(R_{\text{Trp}} + R_{\text{Oxa11}}) = (5 \pm 2) \cdot 10^9 \text{ M}^{-1} \text{ s}^{-1}, \quad (\text{Eq. S6})$$

where we used $D_{\text{Trp}} = 6.6 \cdot 10^{-6} \text{ cm}^2 \text{ s}^{-1}$ and $D_{\text{Oxa11}} = 2.8 \cdot 10^{-6} \text{ cm}^2 \text{ s}^{-1}$ for the diffusion constants of Trp and Oxa11, respectively (50). Based on MD simulations (56), the center-to-center distance between Oxa11 and Trp, $R_{\text{Trp}} + R_{\text{Oxa11}}$, was previously estimated to be 0.7 ± 0.3 nm (50). At a Trp concentration of 6.5 mM, $k_{\text{coll}}^{\text{theo}} = (0.033 \pm 0.013) \text{ ns}^{-1}$, very close to the value of $k_{\text{coll}}^{\text{dyn}}$ observed in the absence of denaturant (Fig. S6B). Since the measured value is within the uncertainty of $k_{\text{coll}}^{\text{theo}}$ (Fig. S6B, shaded band), the dynamic quenching rate is assumed to be a good experimental estimate for diffusion-limited contact formation rate between Oxa11 and Trp. However, with increasing GdmCl concentration, $k_{\text{coll}}^{\text{dyn}}$ deviates from the trend expected if only the increase in solution viscosity is taken into account (Fig. S6B, dashed line), suggesting that GdmCl alters the quenching mechanism (possibly by restricting the accessibility of the two molecules due to preferential interactions with Oxa11 and Trp) and thus leads to an underestimate of the collision rate. We therefore obtain the value of the diffusion-limited collision rate independent of denaturant effects by rescaling the value observed at zero denaturant, $k_{\text{coll}}^{\text{dyn}}(0\text{M})$, by the change in viscosity, i.e. $k_{\text{coll}}^{\text{dyn}*}(c_{\text{GdmCl}}) = k_{\text{coll}}^{\text{dyn}}(0\text{M})\eta(0)/\eta(c_{\text{GdmCl}})$.

The bimolecular collision rates $k_{\text{coll}}^{\text{static}}$ in the presence of 6.5 mM Trp were extracted by analyzing the amplitudes, c_b , and relaxation times, τ_b , of the PET-FCS curves as described in the main text (see section *Contact formation dynamics from PET-FCS*). Bimolecular collision times for the static and dynamic quenching processes can be obtained as the reciprocals of the corresponding rates, $1/k_{\text{coll}}^{\text{static}}$ and $1/k_{\text{coll}}^{\text{dyn}}$, respectively (Fig. S7E). Notably, the static quenching time is greater than the dynamic quenching time at all denaturant concentrations, indicating that static quenching is not diffusion-limited. From the ratios of $k_{\text{coll}}^{\text{static}}$ and $k_{\text{coll}}^{\text{dyn}}$ or $k_{\text{coll}}^{\text{dyn}*}$, respectively, we estimate the corresponding quenching efficiencies, ϕ or ϕ^* , of the reaction-limited contact formation process measured with PET-FCS experiments as a function of GdmCl concentration (see Fig. S7F). As discussed above, $k_{\text{coll}}^{\text{dyn}}$ is likely to reflect not only the simple diffusional

collisions of dye and quencher but to contain contributions from shielding effects of GdmCl. We thus use ϕ^* , which is based on the viscosity-corrected rates, k_{coll}^{dyn*} , to estimate the efficiency of static quenching. Note, however, that ϕ and ϕ^* differ by less than 0.1 in the accessible GdmCl concentration range. This approach results in a value of $\phi^* \approx 50\%$ in the absence of denaturant, compatible with the values between 33% and 50% reported previously for similar oxazine dyes (50). The quenching efficiency decreases monotonically with increasing GdmCl concentration, reaching a value of $\sim 20\%$ at 3.5 M GdmCl (see Fig. 4G inset and SI).

We conducted analogous experiments in the presence of various concentrations of glycerol to investigate the impact of viscosity on the contact formation time and on the quenching efficiency. Based on the analysis of the measured amplitudes and quenching times, we found that the contact formation time is directly proportional to the change in solution viscosity in this case, suggesting that no further correction needs to be included for the quenching efficiency.

PET-FCS measurements of protein L W47C64 in the microfluidic mixer. For PET-FCS experiments in the microfluidic mixer, we took measurements ~ 4 ms after mixing, compared to folding times of ~ 25 ms to ~ 2 s for protein L in the GdmCl concentration range used here (73), corresponding to a fraction of unfolded protein between 92 and 100 %. The stability curve of the Oxa11-labeled protein, obtained by dividing the values of c_q measured at equilibrium by those observed in the microfluidic device (where the protein is completely unfolded), shows a midpoint of ~ 1.8 M GdmCl, very similar to the FRET-labeled variant (1.5 M). The similarity of the stability curves (Fig. 2C) provides additional confirmation that the protein is unfolded at the position where we observe it in the microfluidic device. A small decay component on the microsecond timescale is present even if the quenching Trp is exchanged to Phe in the protein sequence, and its amplitude increases linearly with increasing laser power. Therefore, this contribution is independent of chain dynamics and most likely due to residual triplet state blinking of Oxa11.

PET-FCS measurements of protein L W47C64 as a function of viscosity. Measurements of the contact formation rate in the presence of viscosogens are challenging because increasing concentrations of viscogen decrease the amplitude of the correlation, affecting both the ratio k_+^{obs}/k_-^{obs} (see previous section) and the fraction of unfolded protein, f_u (by stabilizing the folded state). Measurements at high viscosity impair microfluidic mixing experiments owing to high backpressures that limit the concentration range of denaturant that we can investigate. Above 3.5 M GdmCl, correlation amplitudes are too small because GdmCl destabilizes the static complex; below 1.5 M GdmCl, correlation amplitudes are small because the protein is predominantly folded. Therefore, as a compromise between these two limits, we performed the measurements at 2M GdmCl with glycerol as a viscogen. Since the information contained in the quenching amplitude about f_u cannot be disentangled from the ratio of the k_+^{obs}/k_-^{obs} without additional information, we resorted to a different strategy: given the similar stabilities of the FRET and PET constructs (see Fig. 2), we investigated how viscosogens affect the unfolded fraction of the FRET construct. f_u was quantified from the areas of the transfer efficiency peaks corresponding to the unfolded and folded population in single-molecule FRET experiments. We then performed measurements of the PET construct at the same concentrations of glycerol used in the FRET experiments, and by correcting for changes in f_u , we extracted τ_c as a function of viscosity. A linear fit of the viscosity dependence (36) yields $\tau_c = \tau_c^s + \tau_c^i$, where $\tau_c^s = 25 \pm 20$ ns and $\tau_c^i = 180 \pm 40$ ns (see Fig. S14).

Analysis of the MD simulations. Trajectories for protein L, Csp, and ProT α were simulated with the Amber 12 force field and the TIP4P-D water model by Piana *et al.* (31). Atomic

coordinates for the protein were saved with a 1-ns time resolution for a total length of 86 μ s for protein L, 84 μ s for Csp, and 10 μ s for ProT α . Positions of C $^\alpha$ atoms were used to compute distances within the chain, $r_{m,n}^{sim}$ (see Fig. S1); positions of the backbone atoms were used to calculate the dihedral angles, ϕ and ψ . Formation of backbone hydrogen bonds and assignment of secondary structure were obtained using the DSSP algorithm implemented in CAMPARI (74). Salt bridges were identified using cutoff distances of 0.80 nm between the C $^\gamma$ of Asp or the C $^\delta$ of Glu and the N $^\zeta$ of Lys or the C $^\zeta$ of Arg. Interactions between hydrophobic side chains were identified using cutoff distances of 0.90 nm between the C $^\gamma$ of Val, Ile, Leu, Phe, Tyr, and Trp. Cutoff distance were chosen as in reference (14) to facilitate direct comparison. However, the choice of the cutoff distance mainly affects the number of salt bridges and hydrophobic interactions detected and has a relatively small effect on the average relaxation time, indicating that the relaxation times are robust with respect to the cutoff.

Relaxation times of distances, dihedral angles, and hydrogen bonds were obtained by integrating the corresponding time correlation functions, $C(\tau)$, according to

$$\int_0^{\tau_f} (C(\tau) - C(\tau_f)) / (C(0) - C(\tau_f)) d\tau. \tau_f \text{ was chosen as the lag time at which the amplitude of}$$

the correlation function decayed to $1/e^2$ (Fig. S2) to focus on the dominant timescale of unfolded-state relaxation and to reduce the variability of the results due to a variation in integration time and slower dynamic components. Since these values are very similar across correlations of different quantities for the same protein (distances, hydrogen bonds, dihedral angles etc.), the largest τ_f of all correlations was chosen for each protein as the upper limit of integration. The chain reconfiguration time, τ_r , of the distance, r , between residues was calculated from the time correlation function of the distance, $C_r(\tau) = \langle r(t+\tau)r(t) \rangle_t / \langle r(t)^2 \rangle_t$.

The relaxation time for dihedral angles, τ_θ , was calculated by integrating the average of the correlation curves for the ϕ and ψ angles, $C_\phi(\tau) = \langle \phi(t+\tau)\phi(t) \rangle_t / \langle \phi(t)^2 \rangle_t$ and $C_\psi(\tau) = \langle \psi(t+\tau)\psi(t) \rangle_t / \langle \psi(t)^2 \rangle_t$. The relaxation time of hydrogen bonds was obtained from the correlation function $C_{hb}(\tau) = \langle u(t+\tau)u(t) \rangle_t / \langle u(t)^2 \rangle_t$, where $u(t)$ is a function specific to each amino acid and is equal to zero if no hydrogen bonds are formed and equal to 1 if hydrogen bonds are formed at time t . The hydrogen bond map was constructed by averaging the number of hydrogen bonds between each amino acid pair per nanosecond along the trajectory. Similarly, the relaxation times of salt bridges and hydrophobic interactions were obtained from the correlation functions $C_h(\tau) = \langle h(t+\tau)h(t) \rangle_t / \langle h(t)^2 \rangle_t$ and $C_{sb}(\tau) = \langle s(t+\tau)s(t) \rangle_t / \langle s(t)^2 \rangle_t$, where $h(t)$ and $s(t)$ are functions specific to each amino acid pair and are equal to zero if no hydrophobic interaction (h) or salt bridge (s) is formed, and equal to 1 if the salt bridge or hydrophobic interaction is occurring at time t .

The contact formation time was calculated as $\tau_c = \int_0^\infty S(t) dt$, where $S(t)$ is the survival probability of the unquenched state (75):

$$S(t) = \left\langle \exp \left(- \int_{t_0}^{t_0+t} k_0 \theta(R_c - r_{47,64}(\tau)) d\tau \right) f_q \right\rangle_{t_0} / \langle f_q \rangle_{t_0}. \quad \text{Eq. (S7)}$$

$k(r_{47,64}) = k_0 \theta(R_c - r_{47,64})$ describes the distance dependence of the quenching rate between positions 47 and 64 (where Trp and Oxa11 are located), approximated by the Heavyside step function, θ ; k_0 is chosen sufficiently large to recover τ_c to be diffusion-limited (i.e., independent

of k); $f_q = \theta(r_{47,64}(t_0) - R_c)$ is a correction for the (small) fraction of conformations that are in contact at time t_0 ; the contact formation radius, R_c , is the only adjustable parameter. The contact formation time map (Fig. S11 D-F) was constructed assuming $R_c = 0.8$ nm and computing contact formation times for all pairs of amino acids within the chain.

For Csp and protein L, errors for all calculated quantities were assigned by repeating the analysis on 10- μ s segments of the trajectories and calculating mean and standard deviation of the quantity of interest. For ProT α , since the MD simulation is shorter than 10 μ s, the trajectory was split in two, and mean and standard deviation of the quantities of interest were computed for each half. Asymmetric error bands reflect the difference between the value obtained by analyzing the whole trajectory (reported value) or averaging over shorter segments (center of the error interval).

nsFCS correlations from MD simulations. Autocorrelations for the donor and acceptor channels and crosscorrelations were calculated from the simulations (see Fig. 3B) following the approach described previously (67, 76). The photophysics of FRET are described with a kinetic model with three states, corresponding to the ground state (DA), the excited state of the donor (D*A), and the excited state of the acceptor (DA*). The time evolution of the state populations, $\mathbf{p}(t)$, is then given by the rate equation $d\mathbf{p}/dt = \mathbf{K}\mathbf{p}(t)$, where \mathbf{p} is normalized ($\mathbf{1}^T\mathbf{p} = 1$). \mathbf{K} is

$$\mathbf{K} = \begin{pmatrix} -k_{exD} - k_{exA} & k_D & k_A \\ k_{exD} & -k_D - k_F(r) & 0 \\ k_{exA} & k_F(r) & -k_A \end{pmatrix}, \quad \text{Eq. (S8)}$$

where k_{exD} and k_{exA} are the excitation rates for the donor and acceptor; k_D and k_A are the relaxation rates to the ground state; and $k_F(r)$ is the energy transfer rate given by $k_F(r) = k_D (R_0/r)^6$. The distance, r , is obtained from the MD trajectory as a function of time. Since the simulations have a time resolution of only 1 ns, each time step is subdivided into 10 substeps, where the distance is assumed to be constant. With the detection matrices, \mathbf{V}_D and \mathbf{V}_A , which contain the radiative rate constants for the monitored transitions,

$$\mathbf{V}_D = \begin{pmatrix} 0 & k_D & 0 \\ 0 & 0 & 0 \\ 0 & 0 & 0 \end{pmatrix}, \mathbf{V}_A = \begin{pmatrix} 0 & 0 & k_A \\ 0 & 0 & 0 \\ 0 & 0 & 0 \end{pmatrix}, \quad \text{Eq. (S9)}$$

the fluorescence intensity correlations can be computed as ($i = A, D, j = A, D$)

$$g_{ij}(\tau) = \frac{\mathbf{1}^T \mathbf{V}_i e^{\mathbf{K}\tau} \mathbf{V}_j \mathbf{p}_{ss}}{(\mathbf{1}^T \mathbf{V}_i \mathbf{p}_{ss})(\mathbf{1}^T \mathbf{V}_j \mathbf{p}_{ss})}. \quad \text{Eq. (S10)}$$

To account for spectral cross-talk, direct excitation, and the presence of a donor-only species, the correlation is rewritten as a sum of weighted contributions:

$$G_{ij}(\tau) = 1 + a_{ij} \frac{c_d B_{d,i} B_{d,j} g_{i,j}^d(\tau) + c_f B_{f,i} B_{f,j} g_{i,j}^f(\tau)}{(c_d B_{d,i} + c_f B_{f,i})(c_d B_{d,j} + c_f B_{f,j})}, \quad \text{Eq. (S11)}$$

where f and d are the FRET and donor-only populations, respectively. The brightness values are computed as previously (67), with $B_{d,D} = 1$, $B_{f,D} = 1 - E$, $B_{f,A} = \gamma(E + \alpha) + \beta(1 - E)$, and $B_{d,A}$

$= \beta$. The ratio of detection efficiencies of donor and acceptor is $\gamma = 1.13$, the direct excitation of the acceptor is $\alpha = 0.048$, and the crosstalk of donor emission detected in the acceptor channel is $\beta = 0.066$. The relative abundances, c_d and c_f , are estimated from the corresponding transfer efficiency histogram to be $\sim 50\%$. The overall amplitude, a_{ij} , is used as an adjustable parameter.

Tables.

protein L wild type	1	10	20	30	40
	MEEVTIKANL	IFANGSTQTA	EFKGTFEKAT	SEAYAYADTL	
	50	60	64		
	KKDNGE W TVD	VADKGYTLNI	KFAG		
FRET variant (C7-C64)	1	10	20	30	40
	MAHHHHHSAALEVLFQ/GP	MEEVTI C ANL	IFANGSTQTA	EFKGTFEKAT	SEAYAYADTL
	50	60	64		
	KKDNGE W TVD	VADKGYTLNI	KF A C		
PET variant (C64)	1	10	20	30	40
	MAHHHHHSAALEVLFQ/GP	MEEVTIKANL	IFANGSTQTA	EFKGTFEKAT	SEAYAYADTL
	50	60	64		
	KKDNGE W TVD	VADKGYTLNI	KF A C		
control variant (F47-C64)	1	10	20	30	40
	MAHHHHHSAALEVLFQ/GP	MEEVTIKANL	IFANGSTQTA	EFKGTFEKAT	SEAYAYADTL
	50	60	64		
	KKDNGE F TVD	VADKGYTLNI	KF A C		

Table S1. Amino acid sequences of protein L used in this study compared with the wild type sequence. Cys residues (in red) were introduced for labeling with fluorescent dyes (Alexa 488 and Alexa 594 for FRET based experiments, Oxa11 for PET-FCS experiments). For the FRET construct, labeling positions were selected based on previous single-molecule FRET experiments on protein L (37, 38) with the aim of optimizing the separation between folded and unfolded state transfer efficiencies. For measuring contact formation by PET (49), we prepared a single-cysteine variant, G64C, and labeled it with ATTO Oxa11, which is quenched when a complex with the natural tryptophan, W47 (green), is formed. The same Trp residue that acts as a quencher of Oxa11 in the PET construct was used in previous contact formation experiments based on triplet quenching of Trp by Cys (W47-T57C) (18); however, we increased the probe-quencher separation from 10 to 18 amino acids to reduce the relative influence of the Oxa11 linker on the observed dynamics. In the control construct for the PET experiments, Trp is replaced by Phe.

SI Figures

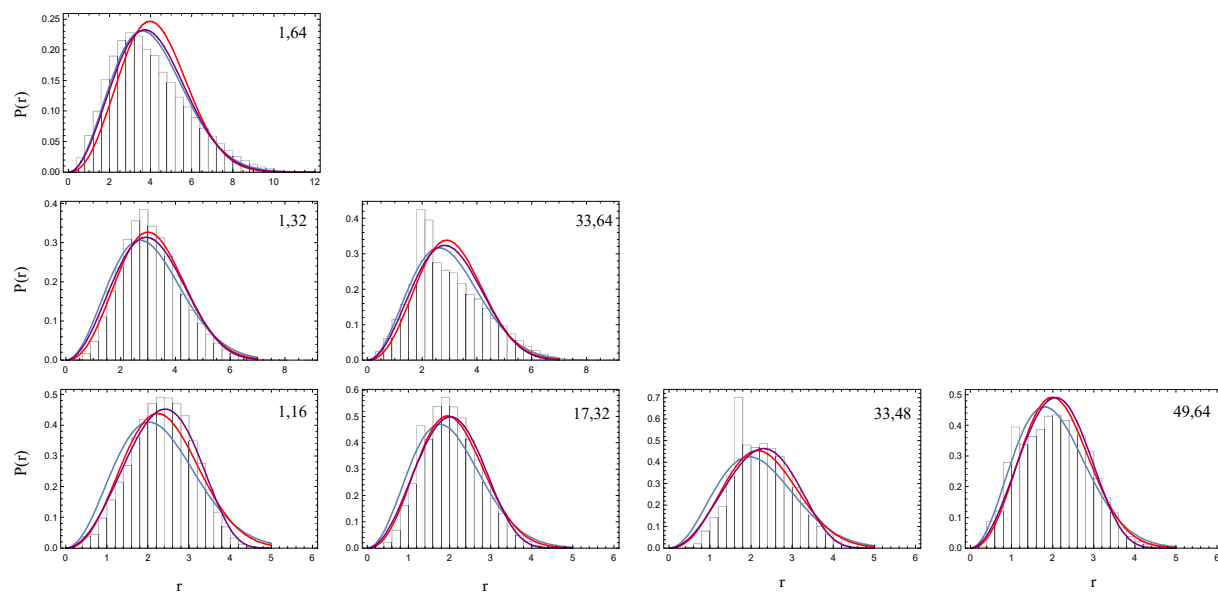


Figure S1. Comparison of distance distributions in MD simulations and polymer models. Distribution of distances between residues m and n (given in upper right corner of each panel) from the MD simulation of unfolded protein L (31) compared to the distance distributions for a Gaussian chain (blue), a self-avoiding-walk (red) and a worm-like chain (purple) with the same root-mean-square distances as the distributions from the simulations to illustrate the level of agreement between atomistic simulations and polymer models.

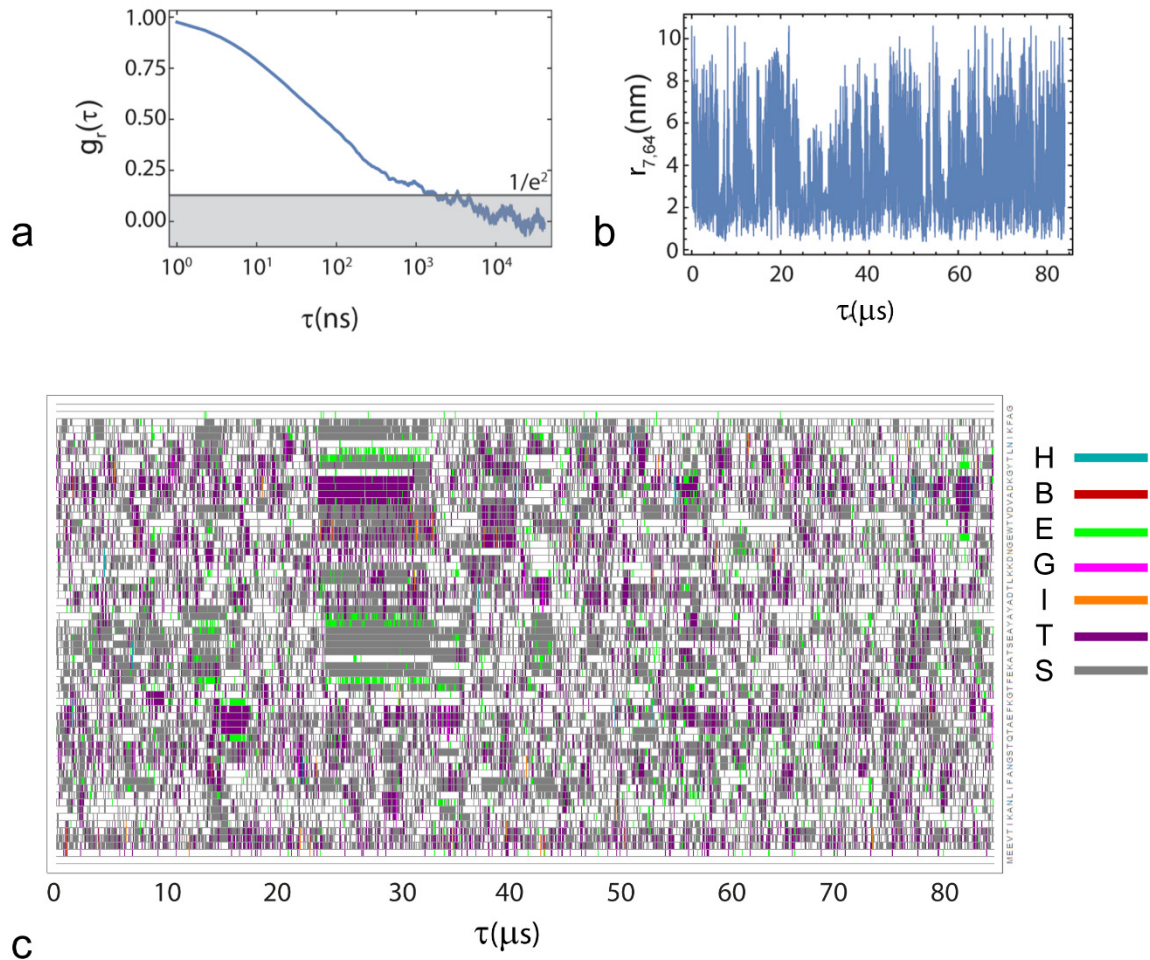


Figure S2. Correlation curve for the distance $r_{7,64}$, the corresponding distance trajectory, and secondary structure assignment from the MD simulation of unfolded protein L. (a) To extract the dominant timescale of chain reconfiguration, the analysis was restricted to the time range corresponding to amplitudes greater than $1/e^2$. (b) Trajectory of the distance $r_{7,64}$. (c) Assignment of secondary structure according to the DSSP algorithm (77) (H: α -helix, B: isolated β -bridge, E: extended/strand, G: 3-helix, I: 5-helix, T: hydrogen-bonded turn, S: bend). Slow dynamics on the timescale of several microseconds reflects the formation of short elements, especially bends, turns, and strands.

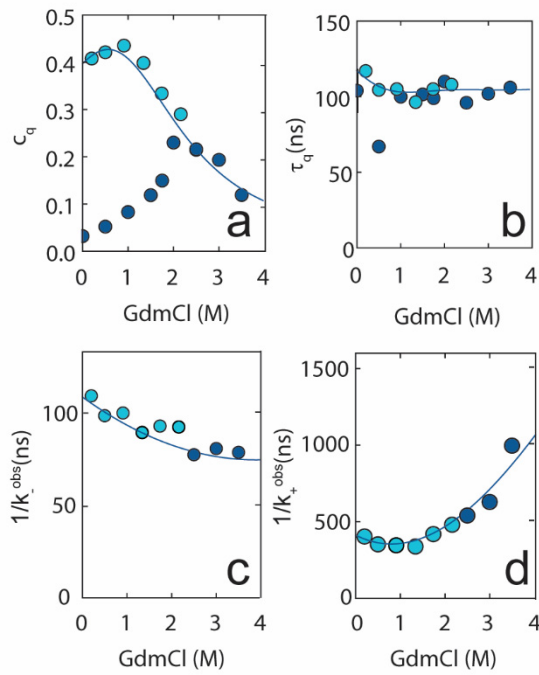


Figure S3. Analysis of PET-FCS curves for unfolded protein L. (A-B) Amplitude, c_q , and relaxation time, τ_q , of the quenching component as measured in the microfluidic device (light blue filled circles) and in equilibrium experiments (dark blue filled circles). Lines are polynomial fits of the data used for interpolation. (C-D) Reciprocal of the observed relaxation rates of forming and breaking the Trp-ATTO Oxa11 complex, k_+^{obs} and k_-^{obs} , respectively, as obtained from c_q and τ_q . Lines are obtained from the polynomial fits of c_q and τ_q .

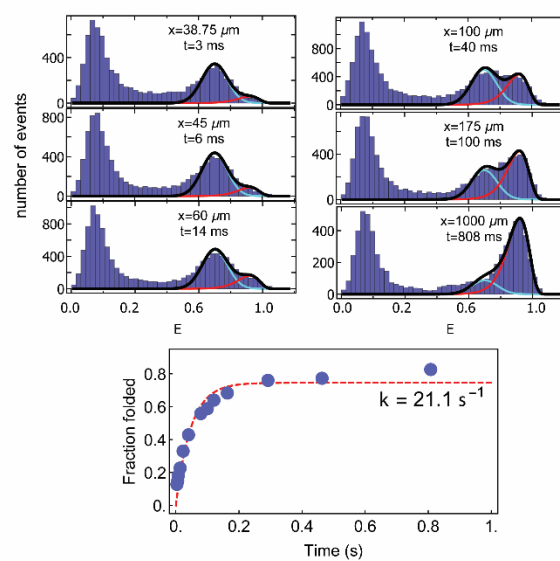


Figure S4. Folding rate measured in the microfluidic mixing device. Transfer efficiency histograms of protein L measured along the observation channel of the microfluidic device at different times (i.e. positions) after the solution is rapidly diluted from 3 M GdmCl to 0.3 M GdmCl with buffer solution (50 mM sodium phosphate pH 7.0). The fraction of folded protein increases with a rate of $21 \pm 3 \text{ s}^{-1}$.

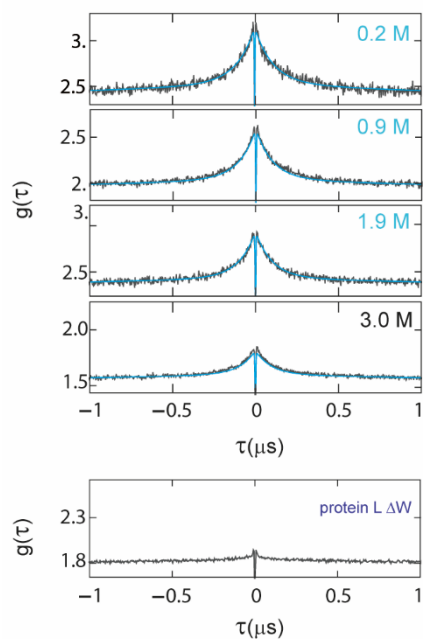


Figure S5. PET-FCS of unfolded protein L. (A) PET-FCS curves of unfolded protein L between $-1 \mu\text{s}$ and $1 \mu\text{s}$ at different GdmCl concentrations. The fast correlated decay on the nanosecond timescale reports on the quenching process, and the amplitude is directly linked to the fraction of unfolded protein and to the stability of the complex. (B) PET-FCS of the control construct of protein L, where the quenching Trp is replaced by Phe (Table S1). The amplitude of the resulting correlation is less than 10% of the amplitude observed in 3.0 M GdmCl.

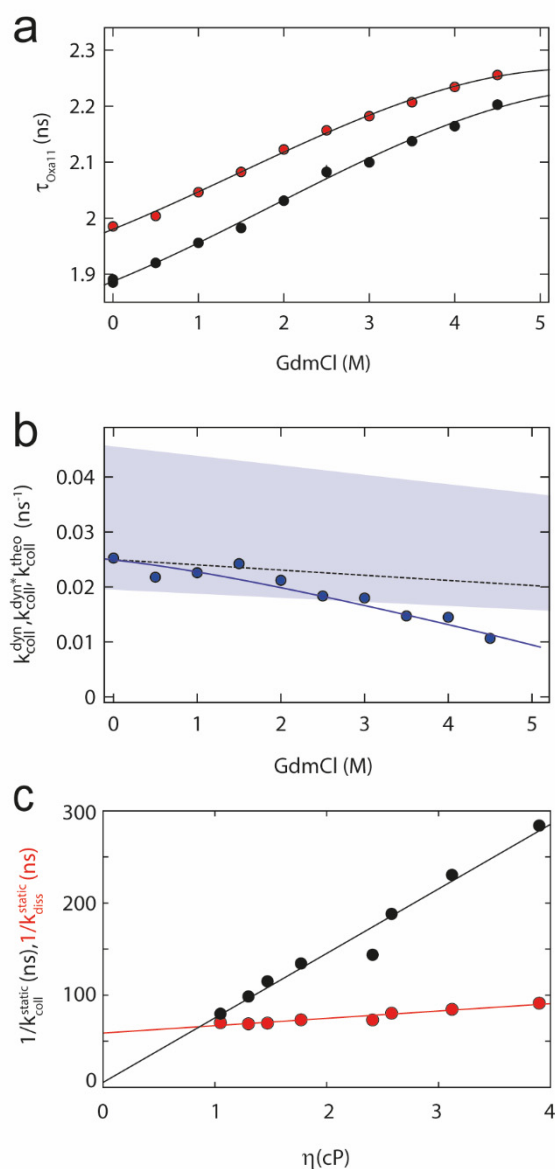


Figure S6. Bimolecular dynamic quenching experiments. (A) ATTO Oxa11 fluorescence lifetime in the presence (black filled circles) and absence (red filled circles) of 6.5 mM Trp as a function of GdmCl concentration. The solid line is a third-order polynomial used for interpolation. (B) Bimolecular collision rates, $k_{\text{coll}}^{\text{dyn}}$ and $k_{\text{coll}}^{\text{dyn}*}$, from fluorescence lifetime-based dynamic quenching experiments (circles) compared to the theoretical estimate $k_{\text{coll}}^{\text{theo}}$ based on Eq. S6, including changes in solvent viscosity (dashed line). The gray band shows the range of the theoretically expected bimolecular collision rate, based on the uncertainty of the contact radius between Oxa11 and Trp (see Eq. S6 and SI Text, *PET-FCS measurements of bimolecular quenching between Trp and ATTO Oxa11*). (C) Solvent viscosity (η) dependence of the bimolecular quenching rate for the formation and dissociation of the static complex, $1/k_{\text{coll}}^{\text{static}}$ and $1/k_{\text{diss}}^{\text{static}}$, respectively, in 100 mM sodium phosphate buffer. The inverse of the rate of complex formation is directly proportional to solvent viscosity, whereas the rate of complex dissociation is much less sensitive to viscosity.

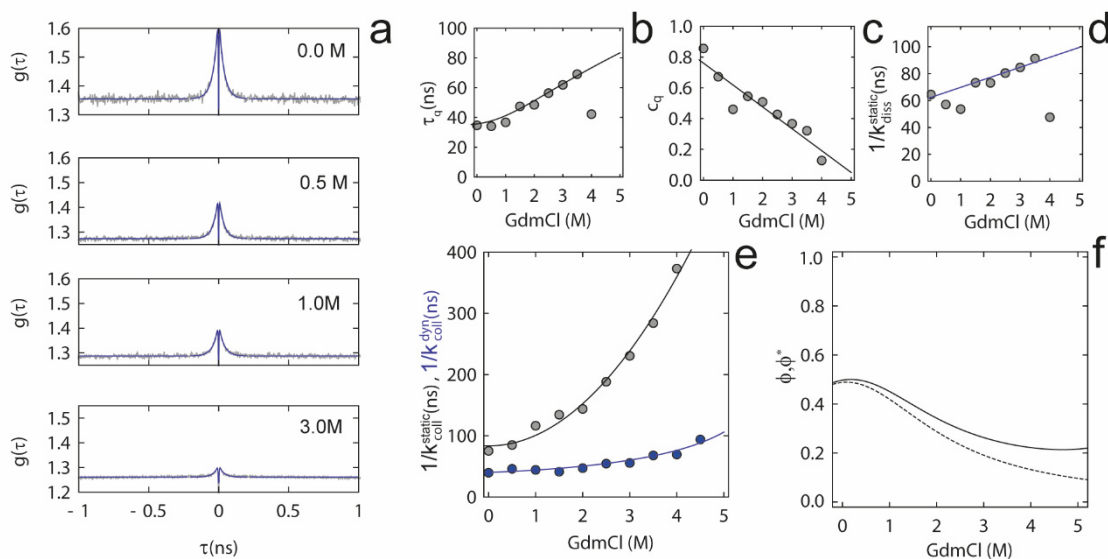


Figure S7. Denaturant dependence of bimolecular PET quenching. (A) Representative PET-FCS curves for bimolecular quenching of free ATTO Oxal11 by 6.5 mM Trp as a function of GdmCl concentration. (B-C) Quenching amplitude, c_q , and decay time, τ_q , as a function of GdmCl concentration. Above 3.5 M GdmCl, c_q becomes too small to be fit reliably. (D) Observed dissociation time of the static Oxal11-Trp complex, $1/k_{diss}^{static}$, as a function of denaturant. (E) Comparison between the bimolecular collision times measured via dynamic quenching, $1/k_{coll}^{dyn}$, (blue filled circles) and static quenching, $1/k_{coll}^{static}$, (gray filled circles). (F) Efficiency of static quenching, ϕ , estimated from the ratio $k_{coll}^{static}/k_{coll}^{dyn}$ using the measured values (solid line), or ϕ^* , using k_{coll}^{dyn} at 0 M GdmCl corrected for the change in solution viscosity (dashed line; cf. dashed line in Fig. S6b).

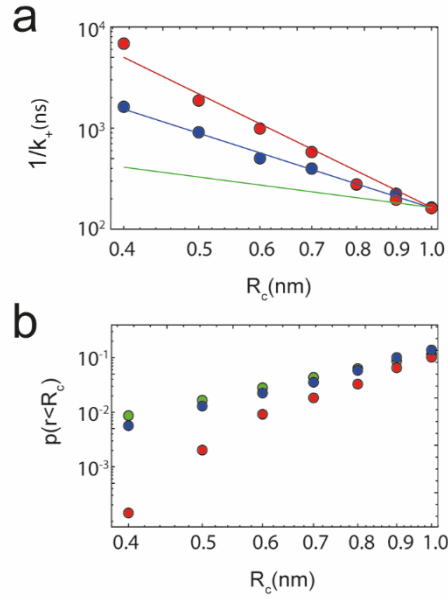


Figure S8. Dependence of the contact formation time, $1/k_+$, on the contact radius, R_c , between the quenching probes for protein L. (A) Contact times between W47 and G64 as calculated from the MD simulation of unfolded protein L (31) according to Eq. S7 for the distance between the C $^\alpha$ atoms of tryptophan and glycine (red filled circles), and between the center of mass of the tryptophan indole ring and the glycine C $^\alpha$ (blue filled circles). Contact times thus exhibit a stronger dependence on R_c than expected from Eq. 2 (green line). (B) Fraction of configurations with distances below R_c for the two cases shown in (A) (red and blue) compared to a Gaussian chain (green). The fraction based on the distance between the tryptophan indole ring and the glycine C $^\alpha$ approaches the trend expected for a Gaussian chain.

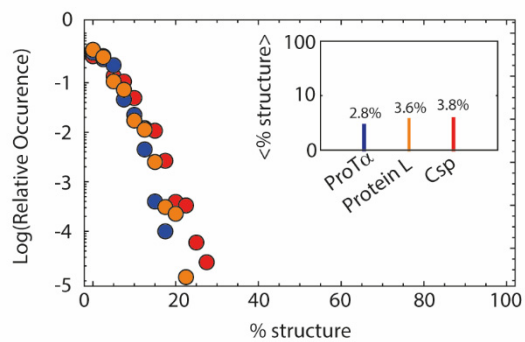


Figure S9. Secondary structure content from MD simulations of unfolded proteins. Relative occurrence of trajectory snapshots containing a specific percentage of residual secondary structure as assigned by the DSSP algorithm (74, 77). Similar values are observed for unfolded Csp (red), protein L (orange), and ProT α (blue). Inset: average percentage of residual secondary structure estimated from the entire trajectory.

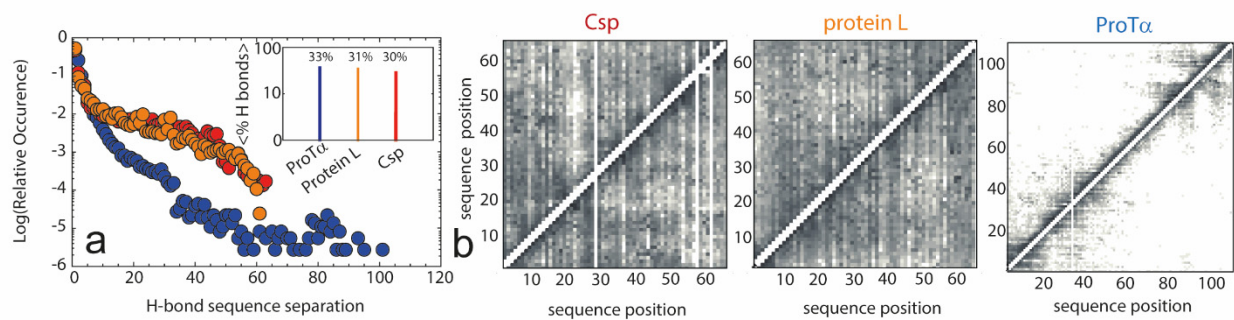


Figure S10. Hydrogen bond formation in unfolded proteins from MD simulations. (A) Occurrence of backbone hydrogen bonds as a function of sequence separation for unfolded Csp (red), protein L (orange), and ProTα (blue) based on the MD simulations (31) and identified using the DSSP algorithm (77). (A, inset) Average percentage of backbone hydrogen bonds present in each snapshot of the MD simulations (relative to all backbone hydrogen bonds identified by DSSP). (B) Map of the occurrence of hydrogen bonds between two amino acids in the MD trajectory (increasing probability from white to dark grey; same scale for all panels).

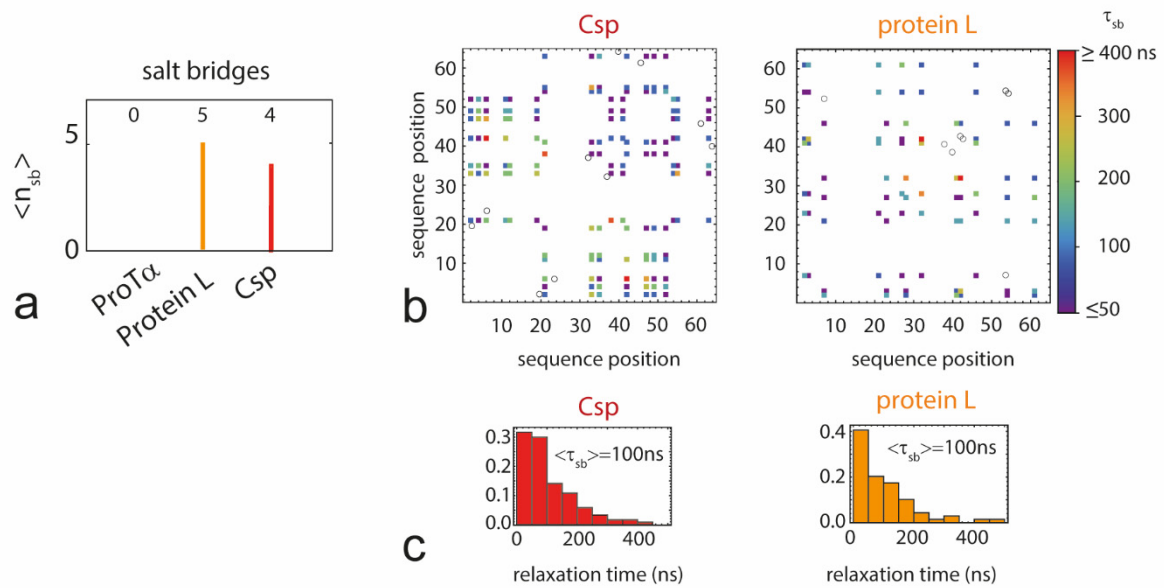


Figure S11. Formation of salt bridges in unfolded proteins from MD simulations. (a) Comparison of the average number of salt bridges per snapshot for ProT α , protein L, and Csp, assuming a cutoff distance of 0.8 nm (see SI Materials and Methods). Note that no salt bridges are detected in the simulation of ProT α . (b) Maps of salt bridges formed during the simulation, colored according to the corresponding relaxation time, τ_{sb} , of the correlation function C_{sb} (see SI Materials and Methods). Black circles correspond to salt bridges found in the native structure. (c) Distributions and mean values of τ_{sb} for protein L and Csp.

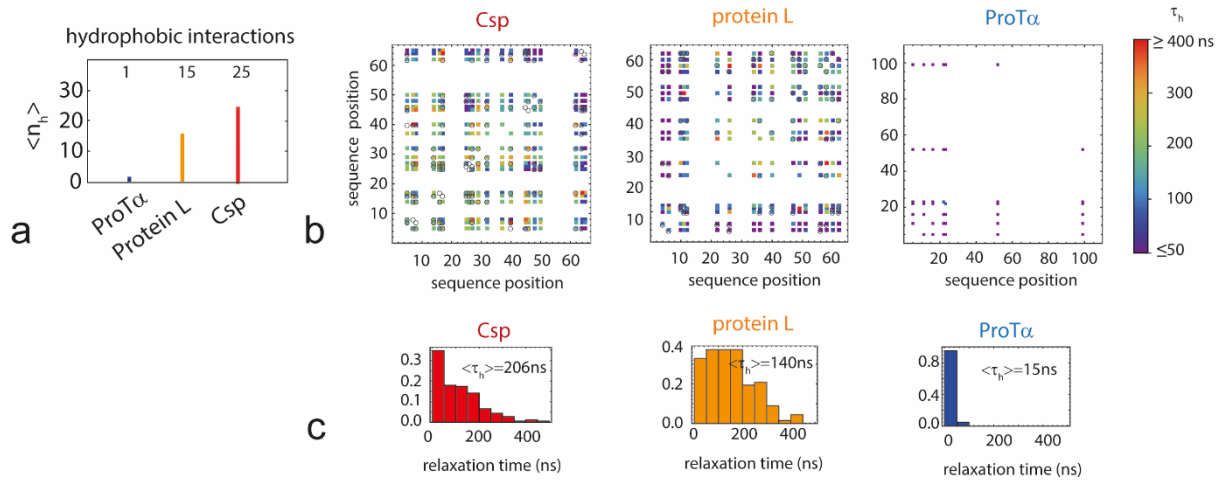


Figure S12. Formation of hydrophobic interactions in unfolded proteins from MD simulations. (a) Comparison of the average number of hydrophobic interactions between amino acid pairs per snapshot for ProT α , protein L, and Csp, using a cutoff distance of 0.9 nm (see SI Materials and Methods). (b) Maps of hydrophobic interactions between amino acid pairs, colored according to the corresponding relaxation time, τ_h , of the correlation function C_h (see SI Materials and Methods). Black circles correspond to hydrophobic interactions in the native structure. (c) Distributions and mean values of τ_h for ProT α , protein L and Csp.

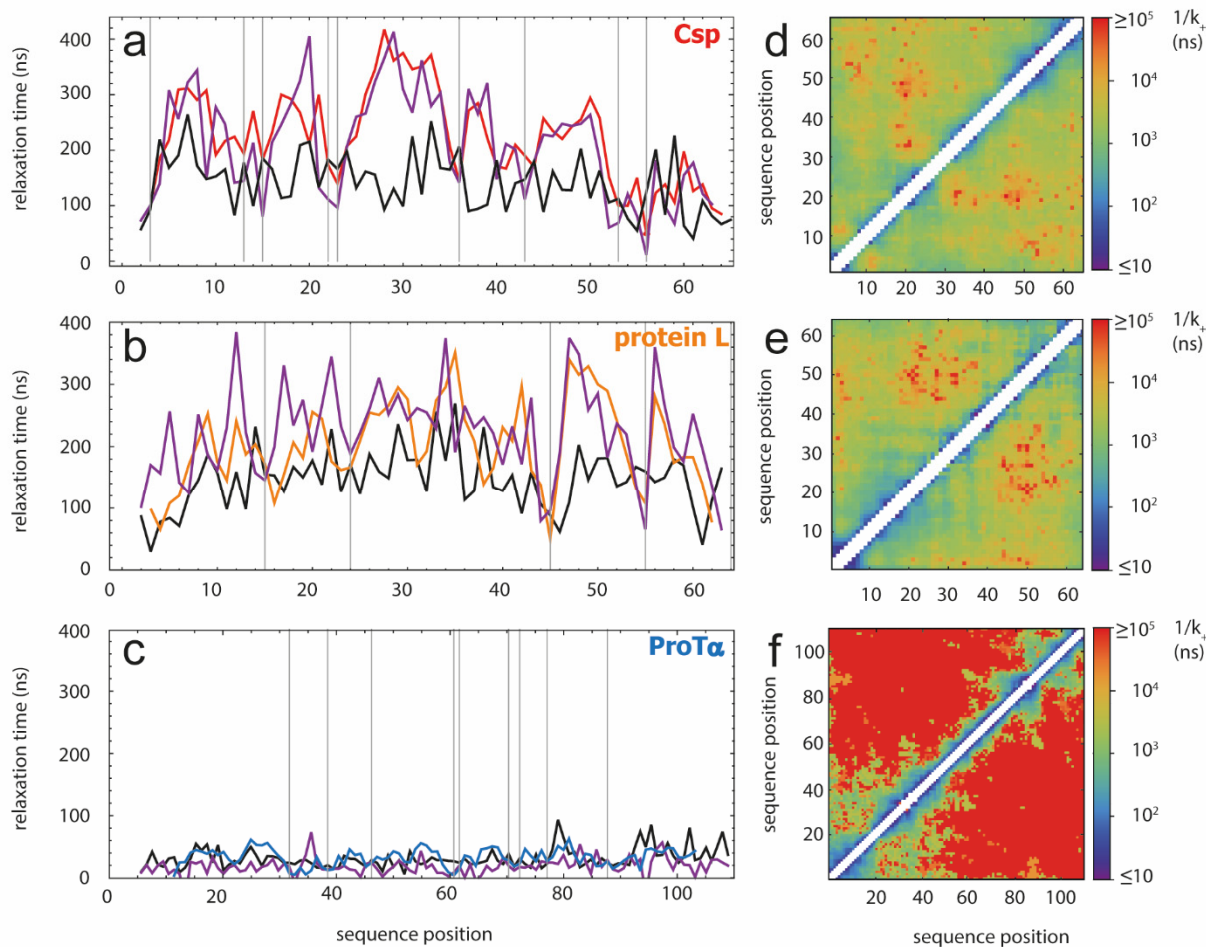


Figure S13. Dynamics of unfolded proteins from MD simulations. (A, B, C) Comparison of relaxation times extracted from the MD simulations (see SI) for the formation of backbone hydrogen bonds between a specific amino acid and the rest of the chain (black line), for the rotation of dihedral angles (purple line), and for the reconfiguration of intrasegment distances of 5-residue segments (approximately a Kuhn segment) for unfolded Csp (red), protein L (orange), and ProTα (blue). Vertical gray lines correspond to the position of glycine residues in the sequence. (D,E,F) Maps of contact formation times for unfolded Csp, protein L, and ProTα.

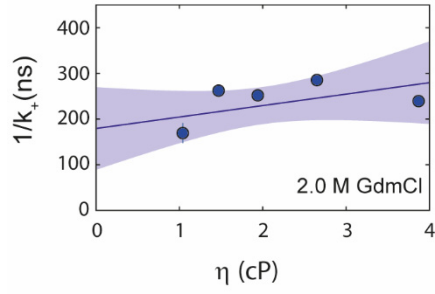


Figure S14. Viscosity dependence of contact formation. Viscosity dependence of the contact formation time, τ_c , in unfolded protein L at 2 M GdmCl as estimated from PET experiments. A linear fit to the data results in $1/k_+ = 1/k_+^s \eta / \eta_0 + 1/k_+^i$ with $1/k_+^i = 180 \pm 40$ ns and $1/k_+^s = 25 \pm 20$ ns, consistent with Eq. 2 when using $R_{47,64} = 4.9$ nm (Fig. 2B), $R_c = 0.8$ nm, and $\tau_i = 42$ ns (see main text). The shaded area corresponds to the 90% confidence interval of the fit.

Supporting references

1. Bryngelson JD, Onuchic JN, Socci ND, & Wolynes PG (1995) Funnels, pathways, and the energy landscape of protein folding: a synthesis. *Proteins* 21:167-195.
2. Dill KA & Chan HS (1997) From Levinthal to pathways to funnels. *Nat. Struct. Biol.* 4:10-19.
3. Camacho CJ & Thirumalai D (1993) Kinetics and Thermodynamics of Folding in Model Proteins. *Proc. Natl. Acad. Sci. USA* 90:6369-6372.
4. Hänggi P, Talkner P, & Borkovec M (1990) Reaction-Rate Theory - 50 Years after Kramers. *Rev. Mod. Phys.* 62:251-341.
5. Pabit SA, Roder H, & Hagen SJ (2004) Internal friction controls the speed of protein folding from a compact configuration. *Biochemistry* 43:12532-12538.
6. Cellmer T, Henry ER, Hofrichter J, & Eaton WA (2008) Measuring internal friction of an ultrafast-folding protein. *Proc. Natl. Acad. Sci. USA* 105:18320-18325.
7. Plaxco KW & Baker D (1998) Limited internal friction in the rate-limiting step of a two-state protein folding reaction. *Proc. Natl. Acad. Sci. USA* 95:13591-13596.
8. Qiu LL & Hagen SJ (2004) Internal friction in the ultrafast folding of the tryptophan cage. *Chem. Phys.* 307:243-249.
9. Ansari A, Jones CM, Henry ER, Hofrichter J, & Eaton WA (1992) The Role of Solvent Viscosity in the Dynamics of Protein Conformational-Changes. *Science* 256:1796-1798.
10. Borgia A, *et al.* (2012) Localizing Internal Friction along the Reaction Coordinate of Protein Folding by Combining Ensemble and Single Molecule Fluorescence Spectroscopy. *Nat. Commun.* 2:1195.
11. Wensley BG, *et al.* (2010) Experimental evidence for a frustrated energy landscape in a three-helix-bundle protein family. *Nature* 463:685-U122.
12. Soranno A, *et al.* (2012) Quantifying internal friction in unfolded and intrinsically disordered proteins with single-molecule spectroscopy. *Proc. Natl. Acad. Sci. USA* 109:17800-17806.
13. Hagen SJ (2010) Solvent viscosity and friction in protein folding dynamics. *Curr. Protein Pept. Sci.* 11:385-395.
14. Chung HS, Piana-Agostinetti S, Shaw DE, & Eaton WA (2015) Structural origin of slow diffusion in protein folding. *Science* 349:1504-1510.
15. Frauenfelder H & Wolynes PG (1985) Rate theories and puzzles of heme protein kinetics. *Science* 229:337-345.
16. Nettels D, Gopich IV, Hoffmann A, & Schuler B (2007) Ultrafast dynamics of protein collapse from single-molecule photon statistics. *Proc. Natl. Acad. Sci. USA* 104:2655-2660.
17. Neuweiler H, Johnson CM, & Fersht AR (2009) Direct observation of ultrafast folding and denatured state dynamics in single protein molecules. *Proc. Natl. Acad. Sci. USA* 106:18569-18574.
18. Waldauer SA, Bakajin O, & Lapidus LJ (2010) Extremely slow intramolecular diffusion in unfolded protein L. *Proc. Natl. Acad. Sci. USA* 107:13713-13717.
19. Schulz JCF, Schmidt L, Best RB, Dzubiella J, & Netz RR (2012) Peptide Chain Dynamics in Light and Heavy Water: Zooming in on Internal Friction. *J. Am. Chem. Soc.* 134:6273-6279.
20. de Sancho D, Sirur A, & Best RB (2014) Molecular origins of internal friction effects on protein-folding rates. *Nat. Commun.* 5.
21. Echeverria I, Makarov DE, & Papoian GA (2014) Concerted Dihedral Rotations Give Rise to Internal Friction in Unfolded Proteins. *J. Am. Chem. Soc.* 136:8708-8713.

22. Sizemore SM, Cope SM, Roy A, Ghirlanda G, & Vaiana SM (2015) Slow Internal Dynamics and Charge Expansion in the Disordered Protein CGRP: A Comparison with Amylin. *Biophys. J.* 109:1038-1048.
23. Schuler B, Hofmann H, Nettels D, & Soranno A (2016) Single-molecule FRET spectroscopy and the polymer physics of unfolded and intrinsically disordered proteins. *Annu. Rev. Biophys.* DOI: 10.1146/annurev-biophys-062215-010915.
24. Zheng WW, De Sancho D, Hoppe T, & Best RB (2015) Dependence of Internal Friction on Folding Mechanism. *J. Am. Chem. Soc.* 137:3283-3290.
25. Zheng WW, de Sancho D, & Best RB (2016) Modulation of Folding Internal Friction by Local and Global Barrier Heights. *J. Phys. Chem. Lett.* 7:1028-1034.
26. Portman JJ, Takada S, & Wolynes PG (2001) Microscopic theory of protein folding rates. II. Local reaction coordinates and chain dynamics. *J. Chem. Phys.* 114:5082-5096.
27. Hofmann H, *et al.* (2014) Role of denatured-state properties in chaperonin action probed by single-molecule spectroscopy. *Biophys. J.* 107:2891-2902.
28. Zerze GH, Mittal J, & Best RB (2016) Diffusive Dynamics of Contact Formation in Disordered Polypeptides. *Phys. Rev. Lett.* 116:068102.
29. Shaw DE, *et al.* (2009) Millisecond-Scale Molecular Dynamics Simulations on Anton. *Proceedings of the Conference on High Performance Computing Networking, Storage and Analysis.*
30. Voelz VA, Singh VR, Wedemeyer WJ, Lapidus LJ, & Pande VS (2010) Unfolded-state dynamics and structure of protein L characterized by simulation and experiment. *J. Am. Chem. Soc.* 132:4702-4709.
31. Piana S, Donchev AG, Robustelli P, & Shaw DE (2015) Water dispersion interactions strongly influence simulated structural properties of disordered protein States. *J Phys Chem B* 119:5113-5123.
32. Best RB, Zheng W, & Mittal J (2014) Balanced Protein-Water Interactions Improve Properties of Disordered Proteins and Non-Specific Protein Association. *J. Chem. Theory Comput.* 10:5113-5124.
33. Vitalis A & Pappu RV (2009) ABSINTH: a new continuum solvation model for simulations of polypeptides in aqueous solutions. *J. Comput. Chem.* 30:673-699.
34. Nerenberg PS, Jo B, So C, Tripathy A, & Head-Gordon T (2012) Optimizing solute-water van der Waals interactions to reproduce solvation free energies. *J. Phys. Chem. B* 116:4524-4534.
35. Huang J, *et al.* (2017) CHARMM36m: an improved force field for folded and intrinsically disordered proteins. *Nat. Methods* 14:71-73.
36. Cheng RR, Hawk AT, & Makarov DE (2013) Exploring the role of internal friction in the dynamics of unfolded proteins using simple polymer models. *J. Chem. Phys.* 138.
37. Sherman E & Haran G (2006) Coil-globule transition in the denatured state of a small protein. *Proc. Natl. Acad. Sci. USA* 103:11539-11543.
38. Merchant KA, Best RB, Louis JM, Gopich IV, & Eaton WA (2007) Characterizing the unfolded states of proteins using single-molecule FRET spectroscopy and molecular simulations. *Proc. Natl. Acad. Sci. USA* 104:1528-1533.
39. Voelz VA, *et al.* (2012) Slow Unfolded-State Structuring in Acyl-CoA Binding Protein Folding Revealed by Simulation and Experiment. *J. Am. Chem. Soc.* 134:12565-12577.
40. Haran G (2012) How, when and why proteins collapse: the relation to folding. *Curr. Opin. Struct. Biol.* 22:14-20.
41. Borgia A, *et al.* (2016) Consistent View of Polypeptide Chain Expansion in Chemical Denaturants from Multiple Experimental Methods. *J. Am. Chem. Soc.* 138:11714-11726.
42. Schuler B, Lipman EA, & Eaton WA (2002) Probing the free-energy surface for protein folding with single-molecule fluorescence spectroscopy. *Nature* 419:743-747.

43. Hoffmann A, *et al.* (2007) Mapping protein collapse with single-molecule fluorescence and kinetic synchrotron radiation circular dichroism spectroscopy. *Proc. Natl. Acad. Sci. USA* 104:105-110.
44. Case DA, *et al.* (2012) AMBER 12 (University of California, San Francisco).
45. Doose S, Neuweiler H, & Sauer M (2009) Fluorescence quenching by photoinduced electron transfer: a reporter for conformational dynamics of macromolecules. *Chemphyschem : a European journal of chemical physics and physical chemistry* 10:1389-1398.
46. Khatri BS & McLeish TCB (2007) Rouse model with internal friction: A coarse grained framework for single biopolymer dynamics. *Macromolecules* 40:6770-6777.
47. Hagen SJ, Hofrichter J, Szabo A, & Eaton WA (1996) Diffusion-limited contact formation in unfolded cytochrome c: estimating the maximum rate of protein folding. *Proc. Natl. Acad. Sci. USA* 93:11615-11617.
48. Krieger F, Fierz B, Bieri O, Drewello M, & Kiefhaber T (2003) Dynamics of unfolded polypeptide chains as model for the earliest steps in protein folding. *J. Mol. Biol.* 332:265-274.
49. Neuweiler H, Schulz A, Bohmer M, Enderlein J, & Sauer M (2003) Measurement of submicrosecond intramolecular contact formation in peptides at the single-molecule level. *J. Am. Chem. Soc.* 125:5324-5330.
50. Doose S, Neuweiler H, & Sauer M (2005) A close look at fluorescence quenching of organic dyes by tryptophan. *Chemphyschem : a European journal of chemical physics and physical chemistry* 6:2277-2285.
51. Wunderlich B, *et al.* (2013) Microfluidic mixer designed for performing single-molecule kinetics with confocal detection on timescales from milliseconds to minutes. *Nature Protocols* 8:1459-1474.
52. Neuweiler H, Lollmann M, Doose S, & Sauer M (2007) Dynamics of unfolded polypeptide chains in crowded environment studied by fluorescence correlation spectroscopy. *J. Mol. Biol.* 365:856-869.
53. Buscaglia M, Lapidus LJ, Eaton WA, & Hofrichter J (2006) Effects of denaturants on the dynamics of loop formation in polypeptides. *Biophys. J.* 91:276-288.
54. Makarov DE (2010) Spatiotemporal correlations in denatured proteins: The dependence of fluorescence resonance energy transfer (FRET)-derived protein reconfiguration times on the location of the FRET probes. *J. Chem. Phys.* 132:035104.
55. Szabo A, Schulten K, & Schulten Z (1980) 1st Passage Time Approach to Diffusion Controlled Reactions. *J. Chem. Phys.* 72:4350-4357.
56. Vaiana AC, *et al.* (2003) Fluorescence quenching of dyes by tryptophan: Interactions at atomic detail from combination of experiment and computer simulation. *J. Am. Chem. Soc.* 125:14564-14572.
57. Lapidus LJ, Eaton WA, & Hofrichter J (2001) Dynamics of intramolecular contact formation in polypeptides: Distance dependence of quenching rates in a room-temperature glass - art. no. 258101. *Phys. Rev. Lett.* 8725:8101-+.
58. Toan NM, Morrison G, Hyeon C, & Thirumalai D (2008) Kinetics of loop formation in polymer chains. *J Phys Chem B* 112:6094-6106.
59. Alexander-Katz A, Wada H, & Netz RR (2009) Internal Friction and Nonequilibrium Unfolding of Polymeric Globules. *Phys. Rev. Lett.* 103.
60. Schulz JCF, Miettinen MS, & Netz RR (2015) Unfolding and Folding Internal Friction of beta-Hairpins Is Smaller than That of alpha-Helices. *J. Phys. Chem. B* 119:4565-4574.
61. Gopich IV, Nettels D, Schuler B, & Szabo A (2009) Protein dynamics from single-molecule fluorescence intensity correlation functions. *J. Chem. Phys.* 131.

62. Müller-Späth S, *et al.* (2010) Charge interactions can dominate the dimensions of intrinsically disordered proteins. *Proc. Natl. Acad. Sci. USA* 107:14609-14614.
63. König I, *et al.* (2015) Single-molecule spectroscopy of protein conformational dynamics in live eukaryotic cells. *Nat. Methods* 12:773-779.
64. Wuttke R, *et al.* (2014) Temperature-dependent solvation modulates the dimensions of disordered proteins. *Proc. Natl. Acad. Sci. USA* 111:5213-5218.
65. de Gennes PG (1979) *Scaling concepts in polymer physics* (Cornell University Press, Ithaca, N.Y.) p 324 p.
66. Müller BK, Zaychikov E, Bräuchle C, & Lamb DC (2005) Pulsed interleaved excitation. *Biophys. J.* 89:3508-3522.
67. Haenni D, Zosel F, Reymond L, Nettels D, & Schuler B (2013) Intramolecular Distances and Dynamics from the Combined Photon Statistics of Single-Molecule FRET and Photoinduced Electron Transfer. *J. Phys. Chem. B* 117:13015-13028.
68. Nettels D, Hoffmann A, & Schuler B (2008) Unfolded Protein and Peptide Dynamics Investigated with Single-Molecule FRET and Correlation Spectroscopy from Picoseconds to Seconds. *J. Phys. Chem. B* 112:6137-6146.
69. Lakowicz JR (2006) *Principles of fluorescence spectroscopy* (Springer, New York) 3rd Ed pp xxvi, 954 p.
70. Schuler B, Müller-Späth S, Soranno A, & Nettels D (2012) Application of confocal single-molecule FRET to intrinsically disordered proteins. *Methods Mol. Biol.* 896:21-45.
71. Sisamakris E, Valeri A, Kalinin S, Rothwell PJ, & Seidel CAM (2010) Accurate Single-Molecule FRET Studies Using Multiparameter Fluorescence Detection. *Methods Enzymol.* 475:455-514.
72. Aznauryan M, *et al.* (2016) Comprehensive structural and dynamical view of an unfolded protein from the combination of single-molecule FRET, NMR, and SAXS. *Proc Natl Acad Sci U S A* 113:E5389–E5398.
73. Scalley ML & Baker D (1997) Protein folding kinetics exhibit an Arrhenius temperature dependence when corrected for the temperature dependence of protein stability. *Proc. Natl. Acad. Sci. USA* 94:10636-10640.
74. Vitalis A & Pappu RV (2009) Methods for Monte Carlo Simulations of Biomacromolecules. *Annual Reports in Computational Chemistry, Vol 5* 5:49-76.
75. Uzawa T, Cheng RR, Cash KJ, Makarov DE, & Plaxco KW (2009) The Length and Viscosity Dependence of End-to-End Collision Rates in Single-Stranded DNA. *Biophys. J.* 97:205-210.
76. Gopich IV & Szabo A (2006) Theory of the statistics of kinetic transitions with application to single-molecule enzyme catalysis. *J. Chem. Phys.* 124.
77. Kabsch W & Sander C (1983) Dictionary of Protein Secondary Structure - Pattern-Recognition of Hydrogen-Bonded and Geometrical Features. *Biopolymers* 22:2577-2637.